Nanoscale

PAPER

View Article Online
View Journal | View Issue

Cite this: *Nanoscale*, 2024, **16**, 11232

Composition-dependent morphologies of CeO_2 nanoparticles in the presence of Co-adsorbed H_2O and CO_2: a density functional theory study

Samuel Moxon, [a] Adam R. Symington,[b] Joshua S. Tse, [a] Joseph M. Flitcroft, [c] Jonathan M. Skelton, [c] Lisa J. Gillie,[a] David J. Cooke,[a] Stephen C. Parker [b] and Marco Molinari *[a]

Received 23rd March 2024,
Accepted 16th May 2024

DOI: 10.1039/d4nr01296h

rsc.li/nanoscale

Catalytic activity is affected by surface morphology, and specific surfaces display greater activity than others. A key challenge is to define synthetic strategies to enhance the expression of more active surfaces and to maintain their stability during the lifespan of the catalyst. In this work, we outline an *ab initio* approach, based on density functional theory, to predict surface composition and particle morphology as a function of environmental conditions, and we apply this to CeO_2 nanoparticles in the presence of co-adsorbed H_2O and CO_2 as an industrially relevant test case. We find that dissociative adsorption of both molecules is generally the most favourable, and that the presence of H_2O can stabilise co-adsorbed CO_2. We show that changes in adsorption strength with temperature and adsorbate partial pressure lead to significant changes in surface stability, and in particular that co-adsorption of H_2O and CO_2 stabilizes the {100} and {110} surfaces over the {111} surface. Based on the changes in surface free energy induced by the adsorbed species, we predict that cuboidal nanoparticles are favoured in the presence of co-adsorbed H_2O and CO_2, suggesting that cuboidal particles should experience a lower thermodynamic driving force to reconstruct and thus be more stable as catalysts for processes involving these species.

Introduction

Cerium dioxide (CeO_2) is a widely-employed catalyst for a number of important chemical processes including those in three-way catalytic converters, solid-oxide electrolyzer cells and the water–gas shift reaction.[1–5] CeO_2 nanoparticles have also shown activity mimicking biological enzymes and have hence been termed "nanozymes".[6–8,115] The catalytic activity of CeO_2 nanoparticles (CeNPs) is determined by their surface composition and reactivity. CeNPs can exhibit many shapes, but most frequently form octahedra (dominant {111} surface), cubes ({100}), and rods ({110}[9] and a mixture of {100} and {111}[10–13] surfaces). The structure and stability of these surfaces is well characterised in the literature.[9–11,14–22] Octahedral CeNPs are the most stable,[13,23–26] and rods and cubes may therefore experience a thermodynamic driving force to reconstruct under certain operating conditions[21,27] (*e.g.* {111} facets appear in rods above 500 K).[28,29] As different particle shapes exhibit different reactivities,[17,30–33] it is essential to control the morphology to ensure the optimum performance of CeO_2-based catalysts and nanozymes.[34]

It has been shown that small-molecule adsorbates such as CO_2 and H_2O can stabilise the {100} facet over the {111} facet and therefore inhibit the formation of more stable octahedral nanoparticles.[25,26,35] The interaction of individual molecules such as H_2O[26,36–40] and CO_2 [25,41–43] with CeO_2 surfaces has thus drawn considerable interest. The behaviour in the presence of CO_2 is critical in automotive three-way catalytic converters, as the reactions progress through surface-bound CO_2.[43–46] H_2O is a ubiquitous surface adsorbate and is also a reactant in the water-splitting reaction in solid-oxide electrolyzer cells, where the reaction pathway has been shown to depend sensitively on the surfaces exposed by the catalyst.[35] CeNPs show enhanced oxidative catalysis in the presence of water molecules,[47] implying that the catalytic performance of CeNPs can be improved in the presence of H_2O. The water-gas shift reaction, which converts CO and H_2O to CO_2 and H_2, relies on the presence of surface-bound H_2O but can be deactivated ("poisoned") by CO_2.[44,48] Given that the {100} surface has a higher affinity for both H_2O[49] and CO_2,[25] control of the dominant facets of the catalyst can have a substantial impact on performance.

While the adsorption of individual molecules on CeO_2 surfaces has been widely studied, despite the importance in cata-

[a]*Department of Physical and Life Sciences, University of Huddersfield, Queensgate, Huddersfield, HD1 3DH, UK. E-mail: m.molinari@hud.ac.uk*
[b]*Department of Chemistry, University of Bath, Claverton Down, Bath, BA2 7AY, UK*
[c]*Department of Chemistry, University of Manchester, Manchester, M13 9PL, UK*

lytic processes the co-adsorption of CO_2 and H_2O has not. To give just one example, the co-adsorption of H_2O and CO_2 is important in the production of syngas, which involves the reduction of stoichiometric CeO_2 followed by re-oxidation using H_2O and CO_2 to produce H_2 and CO.[50–54]

In this work, we outline an approach to predict the surface composition and morphology of CeO_2 nanoparticles as a function of temperature, and H_2O and CO_2 partial pressure based on density functional theory (DFT) calculations. We first compute the adsorption energies of singly- and co-adsorbed CO_2 and H_2O on the stoichiometric and oxygen deficient surfaces of CeO_2 typically expressed by CeNPs. We then proceed to predict the surface compositions, in the form of thermodynamic surface phase diagrams, and the desorption temperatures of the adsorbates, as a function of environmental conditions. Finally, we combine both sets of calculations to predict the thermodynamically stable particle morphologies and surface compositions, and we discuss the implications of our predictions for the design and optimisation of CeO_2-based catalysts.

Computational methodology

DFT calculations were performed using the Vienna *ab initio* simulation package (VASP) code.[55] A plane-wave basis with a cut-off energy of 500 eV was used together with projected augmented-wave (PAW) pseudopotentials[56,57] with frozen cores of [He] for C and O, and [Xe] for Ce. Electron exchange and correlation were treated with the Perdew–Burke–Ernzerhof (PBE) generalised gradient approximation (GGA) functional[58] with the Liechtenstein Hubbard U correction (*i.e.*, PBE+U).[59] In the Lichtenstein model, the coulombic (U) and exchange (J) parameters are treated as independent variables. We chose U = 5 eV and J = 0 eV, which makes the Liechtenstein model equivalent to the Dudarev[60] model with $U_{eff} = U - J = 5$ eV. The use of DFT+U for calculations on CeO_2 is well established in the literature, and our chosen U = 5 eV has been shown to correctly describe the localised Ce^{3+} states in reduced systems.[36,46,61–63] There are other approximations available to study CeO_2, including hybrid functionals and the inclusion of van der Waals interactions,[64–66] but they have been shown to gain similar results to GGA+U for the adsorption of different molecules on CeO_2 surfaces.[41,67]

Bulk CeO_2 and Ce_2O_3

The conventional unit cell of bulk CeO_2 contains four CeO_2 units and has the cubic $Fm\bar{3}m$ space group (no. 225). We obtained an optimised lattice constant of 5.498 Å, which compares well to experimental measurements of 5.412–5.418 Å,[68,69] and computational studies.[116] The Brillouin zone was sampled using a Γ-centred 5 × 5 × 5 k-point grid. The unit cell of bulk Ce_2O_3 includes 16 Ce_2O_3 units and has the $Ia\bar{3}$ space group (no. 206) with an optimised lattice constant of 11.374 Å, which also compares well to the experimental value of 11.126 Å.[70] We have used the cubic bixbyite structure as more representative of the volume expansion associated with the reduction of fluorite CeO_2.[71] The Brillouin zone was sampled using a Γ-centred 4 × 4 × 4 k-point grid. Both structures were minimised using the conjugate gradient method with electronic total energy and ionic force convergence thresholds of 10^{-5} eV and 10^{-3} eV $Å^{-1}$ respectively.

CeO_2 surfaces

CeO_2 surfaces were modelled using the slab method,[72] using models with two identical surfaces separated by a vacuum gap of 15 Å in the direction perpendicular to the surface to avoid interactions between periodic images. The METADISE code[73] was used to generate these model structures, by reorientating bulk CeO_2 so that the surface termination of choice lies perpendicular to the direction of the vacuum gap. The {100}, {110} and {111} surface models are $\sqrt{2} \times \sqrt{2}$, $2 \times \sqrt{2}$ and 1 × 1 expansions of the CeO_2 surface repeat unit, respectively, and the {100} and {110} models are 7 layers thick (28 CeO_2 units) while the {111} model is 5-layers thick (20 CeO_2 units). To quench the dipole on the {100} surface, half the oxygen atoms were transposed from the top to the bottom surface. The size of the slabs used are in line with previous studies,[25,26] and as the slab models do not reconstruct during simulation, they should be sufficient to simulate nanoparticles that remain crystalline and of nanometre scale. However, the effect of the slab thickness on the morphology of nanoparticles should be the focus of future work. The Brillouin zones of all three surface models were sampled using Γ-centred 2 × 2 × 1 k-point grids. The geometries were minimised using the conjugate gradient method with total energy and force thresholds of 10^{-5} eV and 10^{-2} eV $Å^{-1}$. These parameters have previously been used for similar calculations of CeO_2.[26,36]

To generate the O-deficient (reduced) surfaces, an oxygen vacancy was introduced on both sides of the corresponding stoichiometric slab models. Each oxygen vacancy introduces two excess electrons, which localise on surface Ce atoms to create two surface Ce^{3+}. While there is no constraint placed on the position of the Ce^{3+}, our setup ensures that both sides of the slab remain equivalent.

CeO_2 surfaces with adsorbates

The (co-)adsorption of H_2O and/or CO_2 molecules were modelled with different starting configurations to sample adsorption modes. Due to the complex adsorption energy landscape, we only considered those configurations that maximize the hydrogen bond network and the interactions between the adsorbates and surfaces. A complete list of the surfaces we examined is presented in Table 1 together with the labelling scheme used in the discussion. In each entry {*hkl*} are the Miller indices of the surface (*i.e.,* {100}, {110} or {111}), X = S or R denotes a stoichiometric or reduced surface, the molecular formulae indicate the adsorbed species (single adsorption of H_2O and CO_2 or co-adsorption of H_2O–CO_2), and the final letters indicate associative (A), dissociative (D) and/or molecular (M) adsorption of each adsorbate. For example, the associative adsorption of CO_2 on the stoichiometric {111} surface is labelled {111}S-CO_2-A, and the co-adsorption of dissociatively adsorbed H_2O and molecularly adsorbed CO_2 on

Table 1 List of adsorption configurations investigated in this study

Surface	Adsorption description
Bare surface	{*hkl*}X
Single adsorption of CO_2	{*hkl*}X-CO_2-A
	{*hkl*}X-CO_2-M
Single adsorption of H_2O	{*hkl*}X-H_2O-D
	{*hkl*}X-H_2O-M
Co-adsorption of H_2O and CO_2	{*hkl*}X-H_2O-CO_2-DA
	{*hkl*}X-H_2O-CO_2-DM
	{*hkl*}X-H_2O-CO_2-MA
	{*hkl*}X-H_2O-CO_2-MM

the {100} O-deficient surface is {100}R-H_2O-CO_2-DM. In the Results and discussion, we only present the adsorption energies of the most stable configurations (*i.e.* those with the most negative energy of adsorption E_{ads}).

Small molecules

Isolated CO_2, H_2O, and O_2 were modelled in cubic cells with side length 10 Å. These calculations used the same convergence criteria as the surface calculations, with the Brillouin zones sampled at the Γ-point as appropriate for an aperiodic system.

Analysis and imaging

VESTA[75] was used to visualise the models. Data analysis was performed using the Surfinpy code[74,76,77] and the Wulff construction routines in Pymatgen.[78]

Results and discussion

Structure and energetics of bare surfaces

We first examine the bare {100}, {110} and {111} surfaces without adsorbates. The surface energies γ of the bare stoichiometric and O-deficient surfaces were calculated as:

$$\gamma = \frac{1}{2A}\{E_{\mathrm{slab,bare}} - [(n_{\mathrm{CeO_2}} - 2n_{\mathrm{V}})E_{\mathrm{bulk,CeO_2}} + n_{\mathrm{V}}E_{\mathrm{bulk,Ce_2O_3}}]\} \quad (1)$$

where $E_{\mathrm{slab,bare}}$ is the energy of the bare stoichiometric $E^{\mathrm{stoich}}_{\mathrm{slab,bare}}$ or O-deficient slab $E^{\mathrm{O-def}}_{\mathrm{slab,bare}}$ with $n_{\mathrm{CeO_2}}$ CeO_2 formula units and n_{V} oxygen vacancies, $E_{\mathrm{bulk,CeO_2}}$ and $E_{\mathrm{bulk,Ce_2O_3}}$ are the energies per formula unit of bulk CeO_2 and Ce_2O_3, and A is the area of one of the two surfaces of the slab (the factor of two in the denominator arises because there are two identical surfaces in the models). The calculated surface energies of the stoichiometric {100}, {110} and {111} surfaces are 1.45, 1.06 and 0.70 J m^{-2}, respectively, in good agreement with previous literature,[25,36,62] and the calculated γ for the corresponding O-deficient surfaces are 1.42, 1.01 and 0.81 J m^{-2}.

For the O-deficient surfaces, the heat of reduction E_{red} is given by:

$$E_{\mathrm{red}} = \frac{E^{\mathrm{O-def}}_{\mathrm{slab,bare}} + E_{O_2} - E^{\mathrm{stoich}}_{\mathrm{slab,bare}}}{2} \quad (2)$$

where $E^{\mathrm{O-def}}_{\mathrm{slab,bare}}$ and $E^{\mathrm{stoich}}_{\mathrm{slab,bare}}$ are the energies of the bare O-deficient and stoichiometric slabs, E_{O_2} is the energy of an oxygen molecule, and the factor of two accounts for the presence of two oxygen vacancies, one on each side of the slab. We obtain values of E_{red} = 1.69, 1.50 and 2.15 eV for the {100}, {110} and {111} surfaces, respectively, again in[26,36] agreement with the literature.

Adsorption of H_2O and CO_2

The strength with which molecules adsorb at a surface is captured by the adsorption energies E_{ads} defined as:

$$E_{\mathrm{ads}} = \frac{E_{\mathrm{slab,ads}} - \left(E_{\mathrm{slab,bare}} + \sum_i n_i E_i\right)}{\sum_i n_i} \quad (3)$$

where $E_{\mathrm{slab,ads}}$ and $E_{\mathrm{slab,bare}}$ are the energies of the slabs with n_i molecules of species i adsorbed onto the surface and the corresponding bare slabs (whether O-deficient or stoichiometric), respectively, and E_i are the energies of the isolated molecules.

Fig. 1 compares the calculated E_{ads} for the configurations listed in Table 1 for the stoichiometric and O-deficient {100}, {110} and {111} surfaces. In general, associative or dissociative adsorption is stronger than molecular adsorption, with the exception that the {111}S-H_2O-M and {111}S-H_2O-D configurations have similar energies, as highlighted in previous litera-

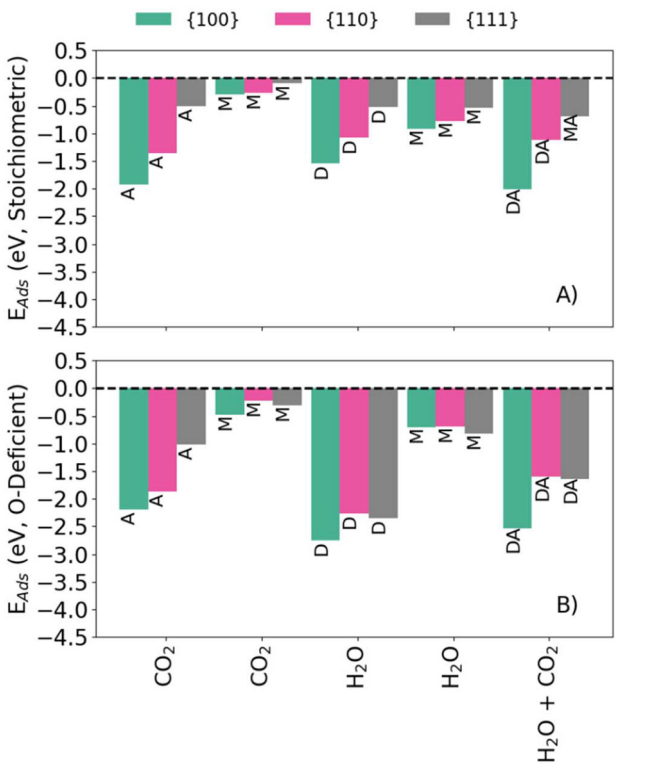

Fig. 1 (Co-)Adsorption energies of H_2O and CO_2 onto stoichiometric (A) and O-deficient (B) {100} (green) {110} (pink) and {111} (grey) CeO_2 surfaces. The labels correspond to those in Table 1.

ture.[36] The adsorption energies of the stoichiometric surfaces follow the order {100} < {110} < {111} (*i.e.*, adsorption at the {100} surface is most favourable), as do the E_{ads} for {*hkl*}R-CO_2-A. On the other hand, the E_{ads} for molecular CO_2 adsorption at the O-deficient surfaces follow the order {100} < {111} < {110} (*i.e.,* adsorption on {111} is more favourable than on {110}). The latter trend has been observed in previous computational studies of H_2O adsorption on ceria.[26] The E_{ads} for {*hkl*} R-H_2O-M follow a different trend with {111} < {100} < {110} (*i.e.,* adsorption is most favourable at the {111} surface).

The co-adsorption energies on the stoichiometric surfaces follow the same general trend of {100} < {110} < {111} as for single adsorption, whereas for the O-deficient surfaces we predict a trend of {100} < {111} ≈ {110}. This might be due to H_2O adsorbing molecularly to the stoichiometric {111} surface but dissociatively to the corresponding O-deficient surface.

Structure and energetics of CO_2 adsorption

The geometries of associatively and molecularly adsorbed CO_2 at the stoichiometric and reduced {100}, {110} and {111} surfaces are compared in Fig. 2. On all six surfaces, associatively adsorbed CO_2 bonds to a surface oxygen to form a CO_3^{2-} (carbonate) ion, and on the O-deficient surfaces the carbonate ions tend to reside close to oxygen vacancies.

The calculated energies of our {*hkl*}S-CO_2-A models are generally in good agreement with the literature,[25] but we obtain a less stable {100}R-CO_2-A configuration (−2.20 eV *vs.* −2.36 eV[25]) and more stable {110}R-CO_2-A and {111}R-CO_2-A configurations (−1.87/−1.02 eV *vs.* −1.56/−0.68 eV[25]). We tentatively attribute these discrepancies to different positions of the oxygen vacancies with respect to the localised Ce^{3+} in our and previous models, but despite multiple attempts, we were unable to reproduce the previous results.

The {100}S-CO_2-A (Fig. 2G) and {100}R-CO_2-A (Fig. 2A) configurations with the most negative E_{ads} comprise flat tridentate carbonate ions.[25,43] The geometry of the {100}S-CO_2-A configuration has been confirmed experimentally using near-edge X-ray absorption fine structure (NEXAFS) measurements, and a previous E_{ads} of −1.93 eV obtained with PBE+U agrees very well with our predicted −1.92 eV.[43] Albrecht *et al.*[43] do not provide geometries for the {100}R-CO_2-M or {100}S-CO_2-M configurations, but they quoted E_{ads} of −0.2 to −0.3 eV that again agree well with our predicted −0.22 and −0.27 eV.

Our {100}R-CO_2-M structure (Fig. 2B) is in good agreement with the similar GGA+U calculations of Zhou *et al.*[79] However, we predict a different {100}R-CO_2-A configuration, which we attribute to a different configuration of the {100} flexible surface oxygen layer.[2,80,81]

XPS measurements by Yang *et al.*[82] indicated that CO_2 adsorbs to the {110} surface as {110}S-CO_2-A, {110}R-CO_2-A, {110}S-CO_2-M or {110}R-CO_2-M, but were unable to determine geometries. We can therefore only compare our {110} configurations to other DFT studies. Our {110}S-CO_2-A model is consistent with that obtained by Symington *et al.*[25] (Fig. 2I) and has a quantitatively similar E_{ads} (−1.35 *vs* −1.32 eV). We also predict a similar {110}R-CO_2-A geometry (Fig. 2C).[25] Other studies have predicted monodentate carbonate species, where one of the O atoms lies in an oxygen vacancy and the other two adopt a "bent" configuration above the surface,[24,42,83] but according to our calculations this configuration is less stable than the bidentate one in Fig. 2C.

Adsorption of CO_2 at the {111} surface has received considerable interest in the context of CO adsorption.[41,45,84,85] We predict a similar {111}S-CO_2-A geometry to Hahn *et al.*[41] and Symington *et al.*[25] (Fig. 2K) and a similar {111}S-CO_2-M configuration to Hahn *et al.*[41] (Fig. 2L). The predicted E_{ads} of our {111}S-CO_2-A model compares well to the value obtained by Symington *et al.* (−0.51 *vs.* −0.52 eV),[25] but we find a more favourable {111}R-CO_2-A configuration with E_{ads} = −1.02 eV compared to −0.68 eV.[25]

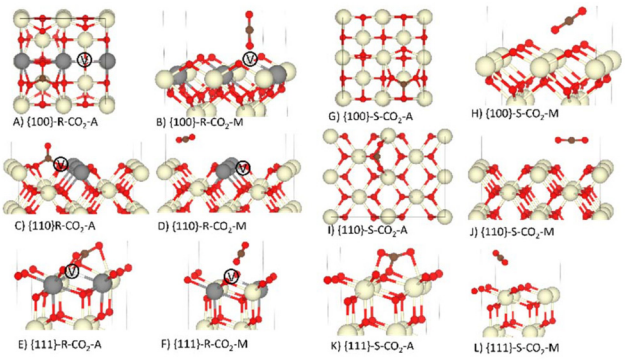

Fig. 2 Associative (A) and molecular (M) adsorption of CO_2 on the O-deficient (R) and stoichiometric (S) {100}, {110} and {111} surfaces of CeO_2. The Ce, O and C atoms are shown in cream, red and brown. In the reduced models, the grey atoms show the positions of the Ce^{3+} and the white atoms marked V show the positions of the oxygen vacancies. Please refer to Table 1 and related text for description of the configurations A-L.

Structure and energetics of H_2O adsorption

The geometries of dissociatively and molecularly adsorbed H_2O on the stoichiometric and O-deficient {100}, {110} and {111} surfaces are shown in Fig. 3. In the {*hkl*}S-H_2O-M and {*hkl*}R-H_2O-M configurations molecular H_2O adsorbs above the surface. On the other hand, in the {*hkl*}S-H_2O-D models the hydroxyl OH bonds to the surface Ce and in the {*hkl*}R-H_2O-D models the OH "heals" the oxygen vacancy. In both models the dissociated H forms a bond with a nearby surface O.

Most experimental and computational studies of H_2O adsorption on CeO_2 surfaces focus on the {111} and {100} surfaces. There is some debate over whether the {111}S-H_2O-A or {111} S-H_2O-M configuration is more stable, with a number of experimental[86,87] and computational[26,36,88] studies finding very similar E_{ads} while other experimental[89,90] and theoretical[37,38,87,88] studies indicate molecular adsorption to be more stable.

The most stable configuration of {111}S-H_2O-M has also been the subject of considerable debate in the computational literature. Some studies predict the most favourable configuration to be the H_2O molecules lying flat on the surface and forming the two H-bonds to surface O atoms, whereas others

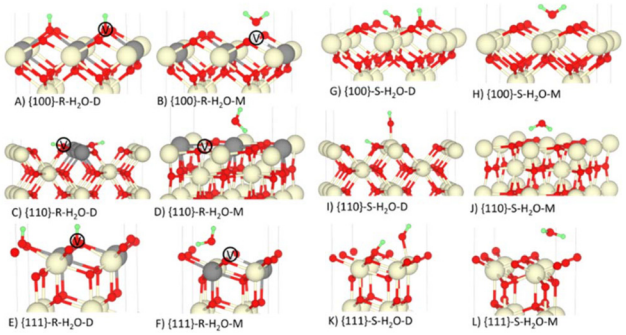

Fig. 3 Dissociative (D) and molecular (M) adsorption of H_2O on the stoichiometric (S) and O-deficient (R) {100}, {110} and {111} surfaces of CeO_2. The Ce, O and H atoms are shown in cream, red and green. In the reduced models, the grey atoms show the positions of the Ce^{3+} and the white atoms marked V show the positions of the oxygen vacancies. Please refer to Table 1 and related text for description of the configurations A-L.

predict a tilted configuration where the molecule forms only one H-bond to be more stable. Molinari *et al.*[36] calculated the E_{ads} for both configurations and found the tilted configuration, equivalent to our {111}S-H_2O-M model (Fig. 3L), had the lowest adsorption energy, albeit with a minimal difference of 0.02 eV.

On the other hand, there is unanimous agreement that the {111}R-H_2O-D is more stable than {111}R-H_2O-M.[26,36,38,87,88,90,91] The temperature-programmed desorption (TPD) and X-ray photoelectron spectroscopy (XPS) experiments performed by Henderson *et al.*[90] found that dissociative adsorption of H_2O at the reduced {111} surface does not result in Ce^{3+} being oxidised, in agreement with our predictions (Fig. 3E). We obtain a more stable {110}R-H_2O-D than in previous studies by Molinari *et al.*[36] and Symington *et al.* (Fig. 3C),[26] which we attribute to a stronger H-bond network in our predicted geometry.

According to O 1s soft XPS (sXPS) measurements by Mullins *et al.*,[86] in an aqueous environment {100}S-H_2O-D dominates over {100}S-H_2O-M, which is consistent with the more favourable predicted E_{ads} for the former (−2.35 *vs.* −0.82 eV). Our predicted geometries and E_{ads} for {100}S-H_2O-D, {100}R-H_2O-D, {100}S-H_2O-M and {100}R-H_2O-M are in good agreement with Molinari *et al.*,[36] and our geometries and E_{ads} for {100}S-H_2O-D and {100}R-H_2O-D similarly agree well with Symington *et al.*[26]

Structure and energetics of the co-adsorption of CO_2 and H_2O

Having demonstrated that our calculations reproduce previous experimental and theoretical results for the single adsorption of CO_2 and H_2O on ceria surfaces, we next considered the co-adsorption of both species (Table 1 and Fig. 4). Co-adsorption is highly likely under experimental conditions, but literature investigating this is much sparser.

In all configurations, the adsorbates were placed to maximise the hydrogen bond network, the interactions between adsorbates, and the interactions between the adsorbates and the surfaces. While we attempted to optimise all possible combinations of dissociative, associative and molecular adsorption of the two molecules, the initial binding configurations were not always retained.

The co-adsorption of CO_2 and H_2O generally appears to have little impact on the local geometries of either species (*cf.* Fig. 2–4). We compute per-adsorbate E_{ads} for co-adsorption (*cf.* eqn (3)), which allows us to compare with the adsorption energies of the individually adsorbed species. If the E_{ads} for a co-adsorbed configuration is lower (more negative) than for an individually adsorbed species, then the adsorption is synergistic and co-adsorption favours the adsorption. On the other hand, if the E_{ads} is higher (more positive) than for an individual adsorption, the adsorption is antagonistic and co-adsorption disfavours the adsorption.

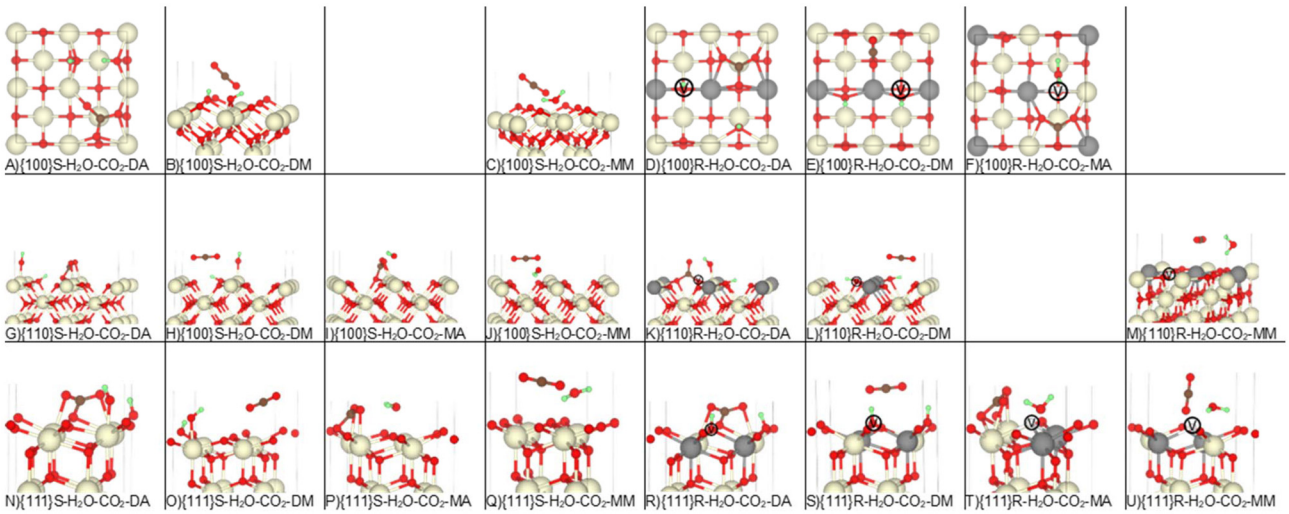

Fig. 4 Co-adsorption of H_2O and CO_2 on the stoichiometric and reduced CeO_2 surfaces. The Ce, O, H and C atoms are shown in cream, red, green and brown. In the reduced models, the grey atoms show the positions of the Ce^{3+} and the white atoms marked V show the positions of the oxygen vacancies. Please refer to Table 1 and related text for description of the configurations A-U.

Despite the minimal structural changes, the dissociative adsorption of H_2O at O-deficient surfaces appears to be destabilised by the presence of CO_2, whereas molecularly adsorbed CO_2 appears to be stabilised by H_2O (Fig. 1). The {100} S-H_2O-CO_2-DA and {110}S-H_2O-CO_2-DA configurations are notable exceptions, with dissociatively adsorbed H_2O stabilising associatively-bound CO_2, and *vice versa*.

In general, the E_{ads} for co-adsorption at different surfaces follow similar trends to single adsorption, *viz.*: (1) adsorption is more favourable at the O-deficient surfaces compared to the stoichiometric surfaces; (2) associative and dissociative adsorption are more favourable than molecular adsorption; and (3) the E_{ads} for the stoichiometric and O-deficient surfaces follow the trend {100} > {110} > {111} and {100} < {111} < {110}, respectively.

Prediction of surface compositions

We now use the calculated surface energies to predict the lowest-energy surface composition, *i.e.,* stoichiometric or O-deficient and with or without adsorbates, as a function of temperature and O_2, H_2O and CO_2 partial pressure. To account for the partial pressures of the adsorbates, eqn (1) is modified to:

$$\gamma = \frac{1}{2A}[E_{slab} - n_{CeO_2}E_{bulk,CeO_2}] - \Gamma_{O_2}[\mu^{\circ}_{O_2}(T) + \Delta\mu_{O_2}] - \sum_i \Gamma_i[\mu^{\circ}_i(T) + \Delta\mu_i] \quad (4)$$

Γ_{O_2} is the surface coverage related to the oxygen surface composition in terms of O_2, and given by:

$$\Gamma_{O_2} = -\tfrac{1}{2A}\tfrac{n_V}{2} \quad (5)$$

This quantity is negative for O-deficient surfaces and nil for stoichiometric surfaces. Γ_i are similarly the surface coverages of the small molecules i:

$$\Gamma_i = \frac{n_i}{2A} \quad (6)$$

$\mu^{\circ}_{O_2}$ is the standard chemical potential of O_2 calculated as:

$$\mu^{\circ}_{O_2}(T) = E_{O_2} + U^{ZPE}_{O_2} + \{[H_{O_2}(T) - H_{O_2}(0)] - TS_{O_2}(T)\} \quad (7)$$

where E_{O_2} and $U^{ZPE}_{O_2}$ are the total energy and vibrational zero-point energy, respectively, evaluated using DFT, and the term in braces is a temperature correction to the Gibbs free energy using experimental data from the NIST database.[92] μ°_i are the standard chemical potentials of the adsorbates calculated as:

$$\mu^{\circ}_i(T) = E_i - TS_i(T) \quad (8)$$

where the temperature correction for the entropy is again obtained from the NIST database.[92] Finally, the $\Delta\mu_{O_2}/\Delta\mu_i$ are externally imposed shifts in the chemical potentials that allow the effect of these variables on the surface composition to be explored. Under the assumption that O_2, H_2O and CO_2 behave as ideal gases, the chemical potentials are related to the partial pressures of the adsorbates as:

$$p_i = \frac{\mu^{\circ}_i(T) + \Delta\mu_i}{k_B T} \quad (9)$$

where k_B is the Boltzmann constant.

We note here two key differences between eqn (1) and (4). First, we consider the formation of O-deficient surfaces *via* loss of surface O as gaseous O_2 rather than formation from a mixture of bulk CeO_2 and Ce_2O_3. This is necessary to account for the effects of temperature and variable O_2 partial pressure in our modelling and is also more realistic, since under most experimental conditions CeO_2 will be in contact with a reservoir of O_2 and not Ce_2O_3. Secondly, we use the chemical potentials of the gaseous adsorbates rather than the DFT energies, which allows us to account for the effects of temperature and variable partial pressures.

Surface composition as a function of $\Delta\mu_{O_2}$ and $\Delta\mu_{CO_2}$ or $\Delta\mu_{H_2O}$

We first map the most stable configurations of the {100}, {110} and {111} surfaces as a function of the chemical potential of O_2 and CO_2 or H_2O (Fig. 5). As expected, high $\Delta\mu_{O_2}$ (high p_{O_2}, oxidising conditions), favours the stoichiometric surfaces, while low $\Delta\mu_{O_2}$ (low p_{O_2}, reducing conditions) favours the O-deficient surfaces. Similarly, high $\Delta\mu_{CO_2}/\Delta\mu_{H_2O}$ favour adsorption of the molecules, as there is an excess of the adsorbates, whereas low $\Delta\mu_{CO_2}$ or $\Delta\mu_{H_2O}$ favour bare surfaces.

We can also use this approach to predict changes to the surface composition with temperature. To do so, we consider temperatures of 298 to 1000 K with the pressures of the gases (*i.e.* p_{O_2} and p_{CO_2}/p_{H_2O}) maintained at a constant 1 bar by varying the corresponding $\Delta\mu_i$. In the presence of CO_2, the most stable surface composition of all the surfaces changes from stoichiometric with associatively adsorbed CO_2 at 298 K to bare stoichiometric surfaces at 1000 K (Fig. 5A–C). In the presence of H_2O the most stable compositions of the {100} and {110} surfaces are predicted to change from stoichiometric with dissociatively-adsorbed H_2O at 298 K to bare stoichiometric at 1000 K (Fig. 5D/E). The {111} behaves similarly but with molecular rather than dissociative adsorption favoured at low temperature (Fig. 5F).

Surface composition as a function of $\Delta\mu_{CO_2}$ and $\Delta\mu_{H_2O}$ at fixed $\Delta\mu_{O_2}$

To consider the co-adsorption of CO_2 and H_2O, we fix the oxygen stoichiometry and predict the most favourable compositions of the stoichiometric and O-deficient surfaces as a function of the chemical potentials of CO_2 and H_2O. To do so, the expression for the surface energies is modified as:

$$\gamma = \frac{1}{2A}\{E_{slab} - [(n_{CeO_2} - 2n_V)E_{bulk,CeO_2} + n_V E_{bulk,Ce_2O_3}]\} - \sum_i \Gamma_i[\mu^{\circ}_i(T) + \Delta\mu_i] \quad (10)$$

This differs from eqn (4) in that we consider the formation of the surfaces from bulk CeO_2 and Ce_2O_3, as we need to fix one of the chemical potentials and we chose to fix $\Delta\mu_{O_2}$.

Fig. 6 shows the most stable surface compositions of the stoichiometric and O-deficient {100}, {110} and {111} surfaces as a function of $\Delta\mu_{CO_2}$ and $\Delta\mu_{H_2O}$. Our calculations lead to three observations: (1) at low $\Delta\mu_{CO_2}$ and $\Delta\mu_{H_2O}$ (*i.e.,* low partial pressures of both adsorbates) the bare surfaces are the most

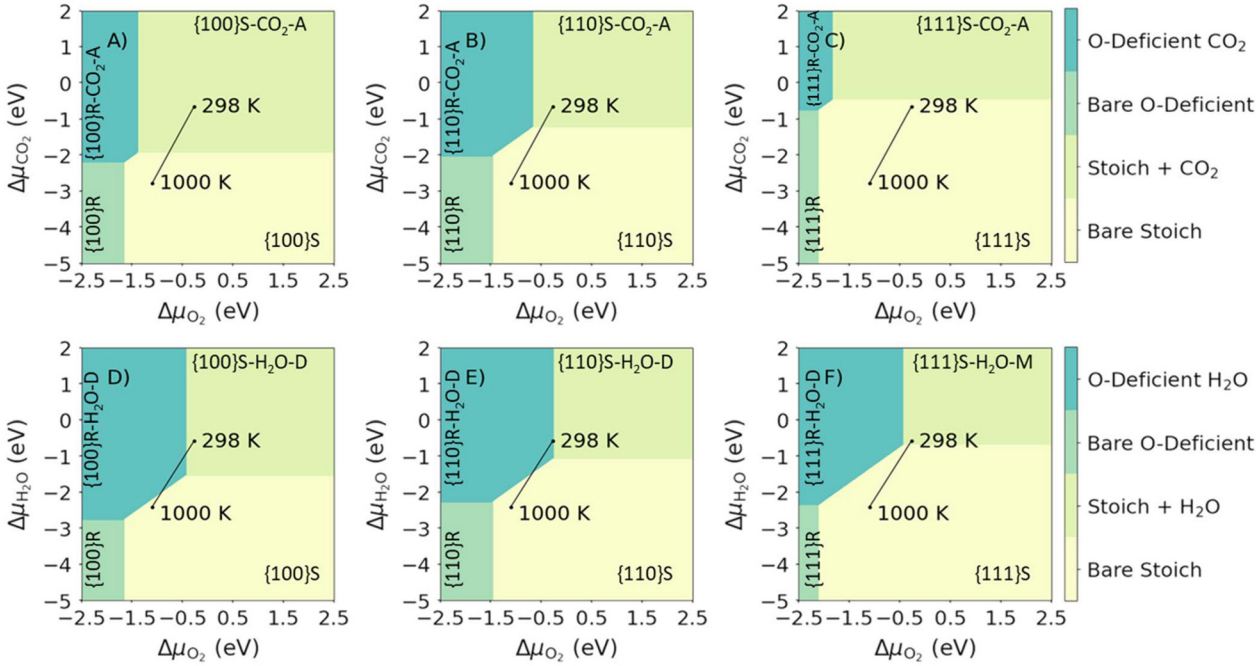

Fig. 5 Surface phase diagrams for the adsorption of single molecules on CeO_2 surfaces. Plots in the top and bottom rows show the most favourable surface compositions as a function of $\Delta\mu_{O_2}$ and $\Delta\mu_{CO_2}$ (top row, A–C) or $\Delta\mu_{H_2O}$ (bottom row D–F). The three columns show the compositions of the {100} (left column, A and D), {110} (centre column, B and E) and {111} surfaces (right column, C and F). The most stable compositions under each set of conditions are indicated using the notation in Table 1. The two points mark the most stable phases with the gases (O_2 and CO_2/H_2O) present at a fixed p = 1 bar, obtained by adjusting the corresponding $\Delta\mu$, at T = 298 and 1000 K, and the connecting line shows the change in composition with temperature.

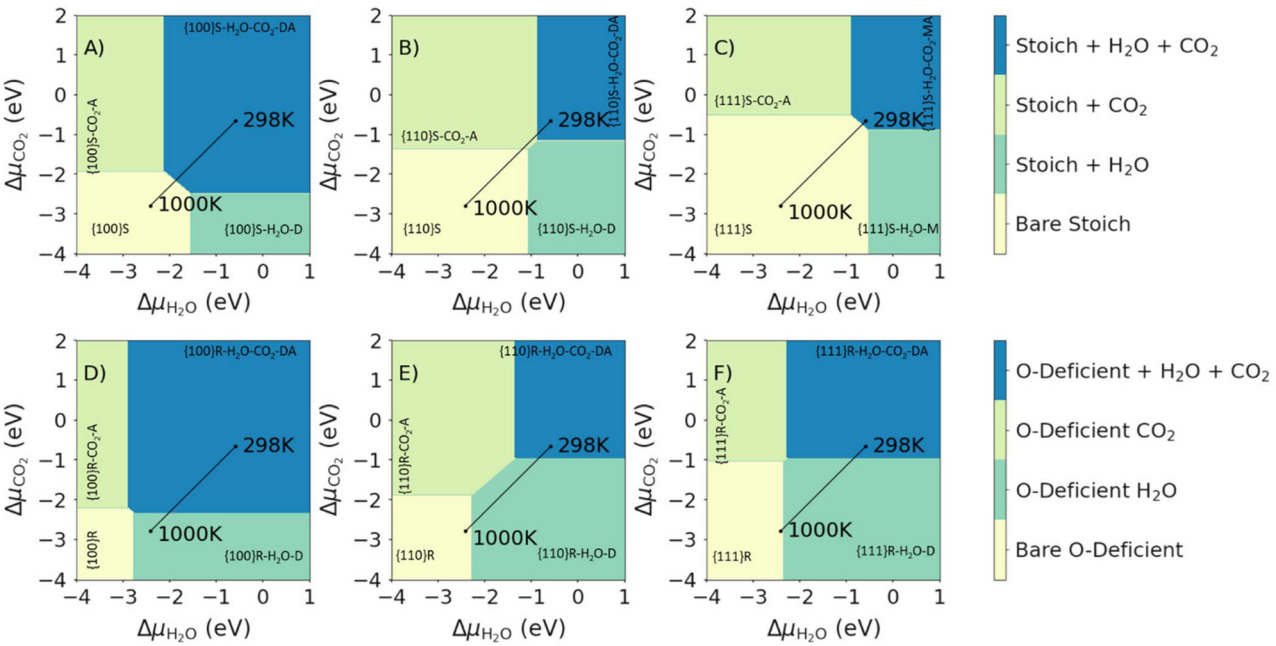

Fig. 6 Surface phase diagrams for the co-adsorption of H_2O and CO_2 on CeO_2 surfaces. Each plot shows the most favourable surface compositions as a function of $\Delta\mu_{H_2O}$ and $\Delta\mu_{CO_2}$. Plots in the top and bottom rows show the most favourable compositions of the stoichiometric (top row, A–C, high $\Delta\mu_{O_2}$) and O-deficient ceria surfaces (bottom row, D–F, low $\Delta\mu_{O_2}$). The three columns show the compositions of the {100} (left column, A and D), {110} (centre column, B and E) and {111} surfaces (right column, C and F). The most stable compositions under each set of conditions are indicated using the notation in Table 1. The two points mark the most stable phases with H_2O and CO_2 present at a fixed p = 1 bar, obtained by adjusting the corresponding $\Delta\mu$, at T = 298 and 1000 K, and the connecting line shows the change in composition with temperature.

stable; (2) at high $\Delta\mu_{CO_2}$ or $\Delta\mu_{H_2O}$ the surfaces with the corresponding adsorbates are the most stable; and (3) at high $\Delta\mu_{CO_2}$ and $\Delta\mu_{H_2O}$, the most stable surfaces are those with both molecules co-adsorbed. At 1 bar p_{CO_2} and p_{H_2O}, we predict that both H_2O and CO_2 are co-adsorbed at 298 K, with molecular or dissociative H_2O and associative CO_2 adsorption. For the O-deficient {100} surface, we predict desorption of CO_2 on heating to 1000 K, while for all other surfaces we predict the desorption of both species on heating.

Prediction of desorption temperatures

In addition to predicting the most favourable surface composition as a function of the chemical potentials (partial pressures) of the adsorbates, it is also useful to predict the desorption temperatures T_D, defined as the highest temperature required to desorb an adsorbate from the surface at a given adsorbate partial pressure.

To do so, we implement a thermodynamic strategy employed successfully in the literature.[25,26,36,93] The energies of the surfaces with adsorbates γ_{ads} can be rewritten as:

$$\gamma_{ads} = \gamma_{bare} + C\left[E_{ads}(T) - RT\ \ln\left(\frac{p_{ads}}{p^\circ}\right)\right] \quad (11)$$

where γ_{bare} is the surface energy of the bare surface, calculated using eqn (1), C is the coverage of the adsorbate(s), and the temperature-dependent adsorption energies $E_{ads}(T)$ are obtained by modifying eqn (3) to include the temperature dependence of the energies of the free adsorbates:

$$E_{ads}(T) = \frac{E_{slab,ads} - \left[E_{slab,bare} + \sum_i n_i E_i(T)\right]}{\sum_i n_i} \quad (12)$$

Here, the $E_i(T)$ are equivalent to the $\mu_i^\circ(T)$ in eqn (8). We then determine the most stable surface (*i.e.,* bare or with (an) adsorbate(s)) as a function of T and p_{ads}. The phase boundary between the bare surfaces and surfaces with adsorbate then determines the T_D at a given p_{ads}. Fig. 7 shows calculations for individually adsorbed H_2O and CO_2 on the three stoichiometric and O-deficient ceria surfaces.

Higher T_D are indicative of stronger adsorption to the surface. In general, we predict higher T_D for the {100} and {110} surfaces compared to the {111} surface, with the notable exception of a higher predicted T_{D,H_2O} for the O-deficient {111} surface than the O-deficient {110} surface (Fig. 7D).

We also predict lower T_D for species adsorbed to the stoichiometric surfaces, in line with previous studies (*cf.* Fig. 7A/B and 7C/D).[2,12,25,26,36,43] The T_D of singly-adsorbed H_2O and CO_2 ($T_{D,H_2O}/T_{D,CO_2}$) have been investigated both computationally[25,26,36,38] and experimentally,[2,43,82,90,91,94–98] but we are not aware of any measurements or predictions for the co-adsorption of the two species.

T_D of CO_2 (T_{D,CO_2})

Table 2 compare our calculated T_D for associatively-adsorbed CO_2 to previous studies. The T_{D,CO_2} for stoichiometric and O-deficient {100} surfaces were measured as 700 and 765 K in ultra-high vacuum (UHV) based on C 1s and O 1s photoemission and C k-edge NEXAFS.[43] The exact pressure is not

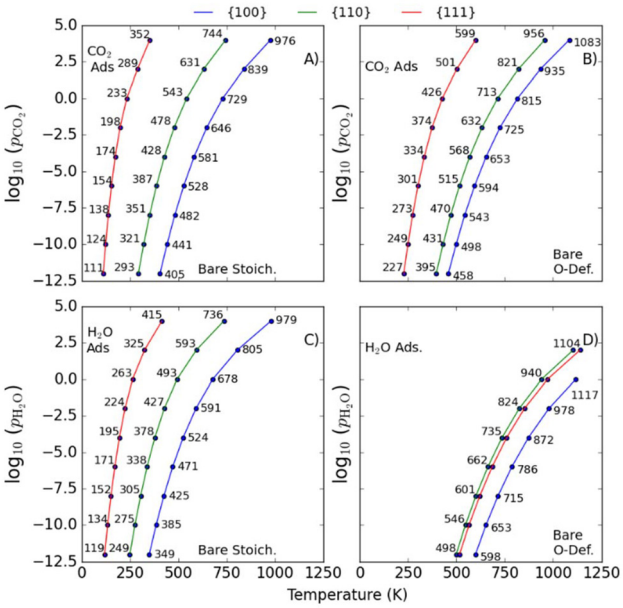

Fig. 7 Predicted desorption temperatures T_D of singly-adsorbed CO_2 (A/B) and H_2O (C/D) at the stoichiometric (A/C) and O-deficient surfaces (B/D) surfaces of CeO_2. Data for the {100}, {110} and {111} surfaces are shown in blue, green and red respectively.

Table 2 Comparison of the predicted desorption temperatures T_D of CO_2 obtained in this study with previous computational and experimental studies. The surface and adsorbate configurations are labelled following the scheme in Table 1

		$\log_{10}(p_{CO_2})$				
Model	Type of study	−12	−10	−7	0	2
{111}S-CO_2-A	Comp. (this study)	111	124	146	233	289
	Comp.[25]	121	133	—	246	292
	Expt.[95]	—	—	<200	—	—
{111}R-CO_2-A	Comp. (this study)	227	249	287	426	501
	Comp.[25]	154	169	—	308	363
	Expt.[95]	—	—	<200	—	—
{110}S-CO_2-A	Comp. (this study)	293	321	369	543	631
	Comp.[25]	289	314	—	535	615
	Expt.[82]	400[a]	—	—	—	—
{110}R-CO_2-A	Comp. (this study)	395	431	493	713	821
	Comp.[25]	338	366	—	615	705
	Expt.[82]	500	—	—	—	
{100}S-CO_2-A	Comp. (this study)	405	441	504	729	839
	Comp.[25]	395	427	—	708	808
	Expt.[43]	—	700	—	—	—
{100}R-CO_2-A	Comp. (this study)	458	498	568	815	935
	Comp.[25]	510	551	—	894	1017
	Expt.[43]	—	765	—	—	—

[a] Ref. 82 quotes a typical pressure of 2×10^{-10} mbar, which we have approximated as $\log_{10}(p_{CO_2}) = -12$.

given, but assuming a "ballpark" $p_{CO_2} \approx 10^{-10}$ bar for UHV measurements, we predict values of 441 and 498 K. The higher values measured experimentally may be due to a higher level of oxygen deficiency in the experimental samples ($CeO_{1.7}$ *vs.* $CeO_{1.93}$ in our O-deficient {100} model). The T_{D,CO_2} for the stoichiometric and O-deficient {110} surfaces were measured UHV to be 400 and 500 K at $p_{CO_2} = 10^{-12}$ bar,[82] and our predicted values are approximately 100 K lower at 293 and 395 K. For the {111} surface we predict T_{D,CO_2} = 146 and 287 K for the stoichiometric and O-deficient surfaces at $p_{CO_2} = 10^{-7}$ bar, which compare relatively well to the T_D < 200 K measured by Senanayake *et al.* under similar conditions.[95] We note however that the experimental T_D of the O-deficient surface may be lower due to the presence of surface oxygen vacancy clusters. Finally, we predict higher T_{D,CO_2} for our {110}R-CO_2-A and {111}R-CO_2-A models but a lower T_{D,CO_2} for our {100}R-CO_2-A configuration compared to a previous study using PBEsol+U,[25] which can be explained by our configurations being lower and higher in energy, respectively.

T_D of H_2O (T_{D,H_2O})

Experimental measurements of T_{D,H_2O} are limited to the {100}[2,98] and {111}[2,90,91,94,96] surfaces. Table 3 compares our predictions to previous computational and experimental studies. Due to the similarity in the adsorption energies of dissociative and molecular H_2O at the {111} surface it is impossible for experiments to study either in isolation, and we instead list the most prevalent configurations. Our predicted T_{D,H_2O} on the stoichiometric and O-deficient {111} surfaces compare well with other literature. We note that Fronzi *et al.*[38] predict higher T_{D,H_2O} for molecularly adsorbed H_2O on the stoichiometric {111} surface than other studies, which we attribute to them considering the chemical potentials of Ce, O and H. Our predictions agree well with other calculations of the T_{D,H_2O} for dissociatively adsorbed H_2O on the stoichiometric {110} surface,[26,36] but we predict higher T_{D,H_2O} for the O-deficient {110} surface due to the more favourable configuration found in the present study. The T_{D,H_2O} for our {100}

Table 3 Comparison of the predicted desorption temperatures T_D of H_2O obtained in this study with previous computational and experimental studies. The surface and adsorbate configurations are labelled following the scheme in Table 1

		Pressure $\log_{10}(p_{H_2O})$				
Model	Type of study	−12	−10	0	1	[b]
{111}S-H_2O-M	Comp. (this study)	119	134	263	291	—
{111}S-H_2O-D	Comp.[26]	154	134	270	—	—
{111}S-H_2O-M	Comp.[36]	150–175	175–200	—	325–350	—
{111}S-H_2O-M	Comp.[38]	330	370	700	—	—
{111}S-H_2O-D[a]	Expt.[2]	—	200–300	—	—	—
{111}S-H_2O-M[a]	Expt.[91]	—	<200	—	—	—
{111}S-H_2O-M	Expt.[90]		—	—	—	320–420
{111}S-H_2O-D[a]	Expt.[94]		—	—	—	300
{111}S-H_2O-M[a]	Expt.[96]		—	—	—	300
{111}R-H_2O-D	Comp. (this study)	516	566	972	1048	—
	Comp.[26]	521	571	837	—	—
	Comp.[36]	500–525	550–575	—	>1000	—
	Expt.[2]	—	>500	—	—	—
	Expt.[91]	—	>500	—	—	—
	Expt.[94]	—	—	—	—	550
	Expt.[96]	—	—	—	—	600
{110}S-H_2O-D	Comp. (this study)	249	275	493	538	—
	Comp.[26]	275	304	462	—	—
	Comp.[36]	275–300	300–325	—	575–600	—
{110}R-H_2O-D	Comp. (this study)	498	546	940	1015	—
	Comp.[26]	349	384	575	—	—
	Comp.[36]	350–375	400–425	—	725–750	—
{100}S-H_2O-D	Comp. (this study)	349	385	678	735	—
	Comp.[26]	382	420	613	—	—
	Comp.[36]	400–425	475–500	—	825–850	—
	Expt.[2,86]	—	<600	—	—	
	Expt.[98]		—	—	—	275
{100}R-H_2O-D	Comp. (this study)	598	653	1117	1204	—
	Comp.[26]	610	667	975	—	—
	Comp.[36]	575–600	400–425	—	>1000	—
	Expt.[2,86]	—	<750	—	—	—

[a] Due to the energetic similarity of the {111}S-H_2O-D and {111}S-H_2O-M configurations it is impractical for experiments to study either in isolation and we therefore list the most prevalent configurations. [b] Exact pressure during the measurements not specified.

S-H_2O-D configuration again compares well with the literature.[36] We predict lower T_{D,H_2O} for dissociatively-adsorbed H_2O at the stoichiometric and O-deficient {100} surfaces than Mullins *et al.*[2,86] which we tentatively attribute to the flexibility of the {100} oxygen sublattice.

T_D of co-adsorbed H_2O and CO_2

To consider desorption of co-adsorbed species we consider two scenarios, *viz.*: (1) selective desorption, where one molecule desorbs and the other remains adsorbed; and (2) simultaneous desorption, where both molecules desorb from the surface. These are illustrated in the reaction schemes shown below:

$$\mathrm{Surf}:\ CO_2 + H_2O \xrightarrow{T_{D-sel-CO_2}} \mathrm{Surf}:\ H_2O + CO_2(g) \quad (13)$$

$$\mathrm{Surf}:\ CO_2 + H_2O \xrightarrow{T_{D-sel-H_2O}} \mathrm{Surf}:\ CO_2 + H_2O(g) \quad (14)$$

$$\mathrm{Surf}:\ CO_2 + H_2O \xrightarrow{T_{D-sim-CO_2/H_2O}} \mathrm{Surf} + CO_2(g) + H_2O(g) \quad (15)$$

Selective desorption of CO_2 or H_2O

It is also useful to define a shift in desorption temperature, ΔT_D, as the difference between the T_D for selective desorption when two co-adsorbed and the T_D of the singly adsorbed species:

$$\Delta T_{D\text{-sel-}i} = T_{D\text{-sel-}i} - T_{D,i} \quad (16)$$

$\Delta T_{D\text{-sel-}i} > 0$ indicates that the presence of the co-adsorbed molecules stabilises the adsorption (*i.e.,* there is a synergistic interaction between the adsorbates), while $\Delta T_{D\text{-sel-}i} < 0$ implies the opposite (*i.e.,* an antagonistic interaction).

We find that the presence of both adsorbates has a destabilising effect on both the stoichiometric and O-deficient {110} surface (*i.e.,* $\Delta T_{D\text{-sel-}CO_2}$ and $\Delta T_{D\text{-sel-}H_2O} > 0$) but a stabilising effect on both stoichiometric and O-deficient {100} surfaces ($\Delta T_{D\text{-sel-}CO_2} < 0$ and $\Delta T_{D\text{-sel-}H_2O} < 0$; Fig. 8A–D). On the other hand, we see a synergistic stabilising effect on the stoichiometric {111} surface (Fig. 8A/C) but an antagonistic effect on the O-deficient {111} surface (Fig. 8B/D).

Simultaneous desorption of CO_2 and H_2O

As for single adsorption, the T_D for simultaneous desorption represents the highest temperature at a given set of adsorbate partial pressures required for both co-adsorbed molecules to desorb together, and thus define a phase boundary between a bare surface and a surface with both species co-adsorbed.

The predicted $T_{D\text{-sim-}CO_2/H_2O}$ for the O-deficient surfaces is larger than for the stoichiometric surfaces, indicating that it is easier to simultaneously desorb H_2O and CO_2 from the stoichiometric surfaces than the O-deficient surfaces (Fig. 8E/F). The predictive $T_{D\text{-sim-}CO_2/H_2O}$ for the stoichiometric surfaces fall in the order of {100} > {110} > {111} (Fig. 8E), while the T_D

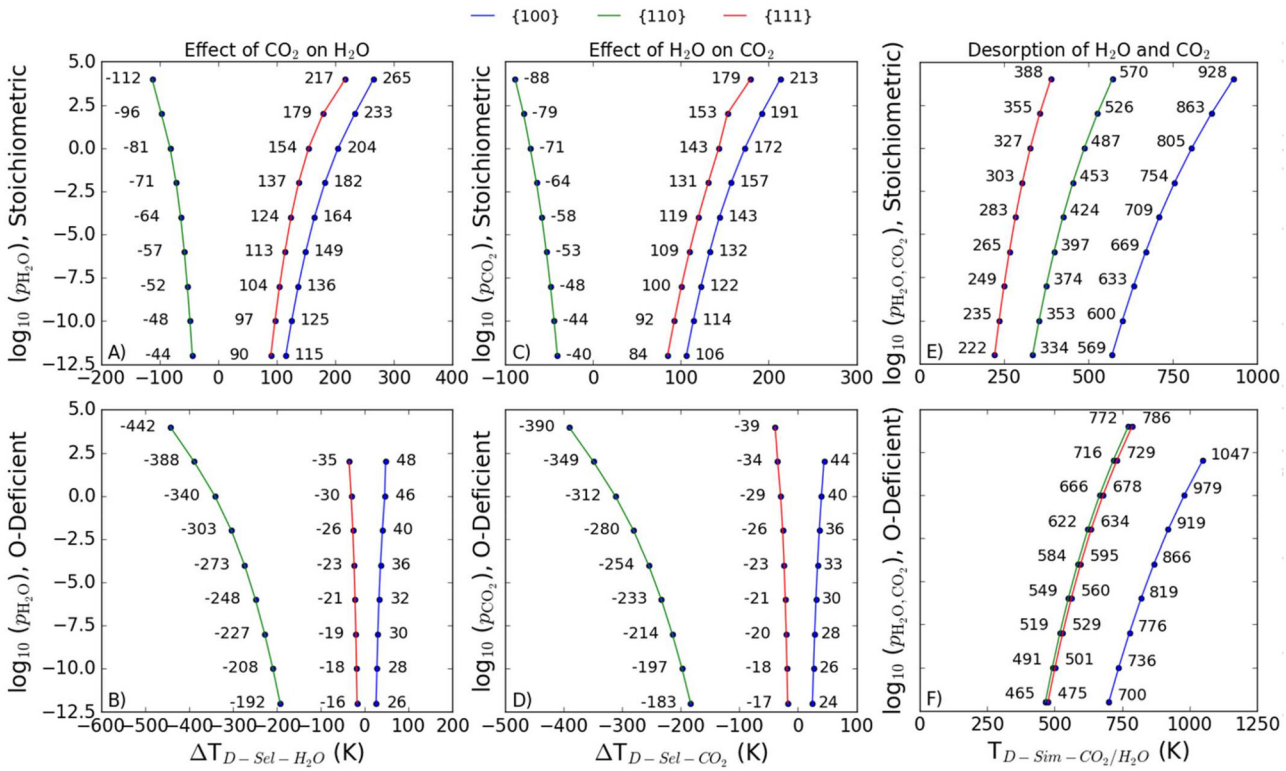

Fig. 8 Predicted desorption temperatures T_D for the selective and simultaneous desorption of H_2O and CO_2 from CeO_2 surfaces as a function of the adsorbate partial pressure(s). For selective desorption, we plot the shift ΔT_D relative to the T_D of singly-adsorbed molecules. The two rows of plots show predictions for the stoichiometric (top row, A/C/E) and O-deficient (bottom row, B/D/F) {100} (blue), {110} (green) and {111} (red) surfaces. The three columns show the effect of CO_2 on the desorption of H_2O (A/B), the effect of H_2O on the desorption of CO_2 (C/D), and the predicted T_D for simultaneous desorption of both species (E/F).

Table 4 Comparison of the desorption temperatures T_D for selective and simultaneous desorption of CO_2 and H_2O from the stoichiometric and O-deficient {100}, {110} and {111} ceria surfaces at a reference p_{CO_2}/p_{H_2O} = 1 bar

		Stoichiometric			O-deficient		
Reference	Partial pressure	{111}	{110}	{100}	{111}	{110}	{100}
T_{D,CO_2}	p_{CO_2} = 1 bar	234	543	730	713	427	730
T_{D,H_2O}	p_{H_2O} = 1 bar	264	494	678	972	941	1118
$T_{D\text{-sim-}CO_2/H_2O}$	$p_{CO_2} = p_{H_2O}$ = 1 bar	328	487	806	679	666	980
$T_{D\text{-sel-}CO_2}$	p_{CO_2} = 1 bar	377	472	902	397	401	856
$T_{D\text{-sim-}H_2O}$	p_{H_2O} = 1 bar	418	412	883	941	600	1164

from the O-deficient {110} and {111} surfaces are reversed to give an order of {100} > {111} > {110} (Fig. 8F).

Comparison of selective and simultaneous desorption

It is of interest to compare the desorption temperatures for selective and simultaneous desorption, as in catalytic processes involving both species the temperature and partial pressure of the gases should be optimised to ensure the required species are present on the surface. As a reference point, Table 4 summarises the calculated T_D for the singly-adsorbed and co-adsorbed molecules for each of the stoichiometric and O-deficient surfaces at a reference p_{CO_2}/p_{H_2O} = 1 bar.

For both the stoichiometric and O-deficient {110} surfaces, the predicted $T_{D\text{-sim-}CO_2/H_2O}$ are higher than the T_D for selective desorption, indicating the molecules will desorb selectively rather than simultaneously. The reverse is true for the stoichiometric {111} and {100} surfaces, for which the calculations predict it is more favourable for both molecules to desorb simultaneously. On all three O-deficient surfaces, the $T_{D\text{-sel-}CO_2}$ are the lowest, suggesting CO_2 would likely desorb first, whereas on the stoichiometric {110} surface the $T_{D\text{-sel-}H_2O}$ is the lowest, suggesting H_2O would desorb first.

Surface area and morphology

We now utilise our predicted surface free energies and desorption temperatures to predict the equilibrium surface composition and, hence, the morphology of CeNPs as a function of temperature and adsorbate partial pressure. We begin by predicting the relative areas of the {111}, {110} and {100} surfaces taking into consideration the T_D of the adsorbates and the impact of the molecules on the surface energies. The effect of different conditions on the relative areas can be most conveniently visualised in the form of "surface area" phase diagrams showing the proportions of the different surfaces, and whether bare or with adsorbed species, as a function of temperature and/or adsorbate partial pressure(s).

Relative surface areas in the presence of CO_2

Fig. 9A shows the predicted area ratio of the {100}, {110} and {111} surfaces in stoichiometric CeNPs as a function of temperature and p_{CO_2}. We also show on these plots the predicted T_{D,CO_2} of the three surfaces, which provides an indication of whether CO_2 would be adsorbed under a given set of conditions. Under most conditions, we predict that the CeNPs are

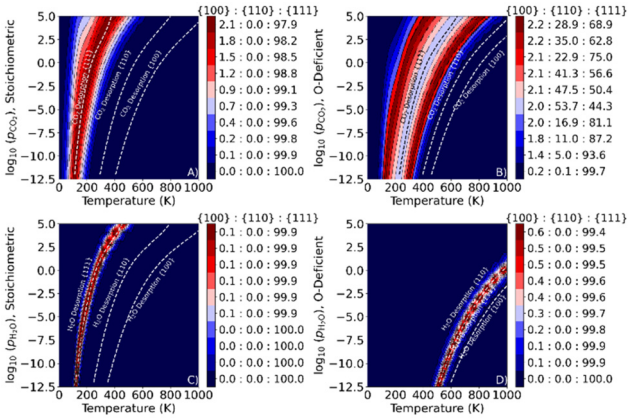

Fig. 9 Predicted ratios between the {100}, {110} and {111} surfaces as a function of temperature and p_{CO_2} (A/B) or p_{H_2O} (C/D) for stoichiometric (A/C) and O-deficient (B/D) CeO_2 nanoparticles. The white dotted lines represent the predicted desorption temperatures of CO_2/H_2O from the surfaces to indicate the surface speciation.

dominated by the {111} surface, corresponding to an octahedral morphology. However, over a narrow range of temperatures around the T_{D,CO_2} for the {111} surface, we predict a small proportion of the {100} surface, which would produce the truncated octahedral shape predicted by Symington *et al.*[25] The dominant {111} composition, together with T_{D,CO_2} being lowest at this surface, additionally indicates that at high T the CeNPs are predicted to present bare surfaces.

Fig. 9B shows our predictions for O-deficient CeNPs. At the extremes of temperature (*i.e.,* low and high T), we again predict the {111} surface to be dominant. However, around T_{D,CO_2} for the {111} surface, the area of the {110} is predicted to increase to just over half of the total ratio, yielding an octahedron with flat edges. These differences in surface composition result in CO_2 being adsorbed over a wider range of temperatures than for stoichiometric NPs. We predict a greater dominance of the {110} surface than Symington *et al.*,[25] which we attribute to our lower-energy {110}R-CO_2-A configuration. Symington *et al.* also predict a higher proportion of the {100} surface than in this study, which we put down to them considering higher CO_2 coverage and finding a lower-energy configuration with two CO_2 molecules adsorbed to the surface.

Barroso Bogeat *et al.* found that ceria nanocubes interact strongly with CO_2,[99] and that the redox properties of the nano-

cubes can be improved by forming {111} dominated pyramids.[13] Hashimoto *et al.*[100] reported that catalytic behaviour to CO_2 methanation falls in the order of {110} > {100} > {111} for cubic, rod-like and octahedral NiO_x-decorated CeO_2 nanostructures, which they attributed to the enhanced reactivity of oxygen atoms on the {110} surface compared to the {100} and {111} surfaces. This is corroborated by DFT calculations indicating a lower reduction energy at the {110} surface[26,36,101,102] and classical molecular dynamics simulations indicating easier reconstruction and faceting of the {110} compared to the {100} and {111} surface.[17] Therefore, when designing a catalyst for CO_2 activation, an oxygen deficient material with large {100} facets and wide {110} edge surfaces is likely to be optimal. This is supported by the IR measurements by Wu *et al.*,[45] which demonstrated that carbonates are less strongly adsorbed to the less reactive octahedral nanoparticles (dominant {111}) than to the more active rods and cubes (dominant {100} and {110}).

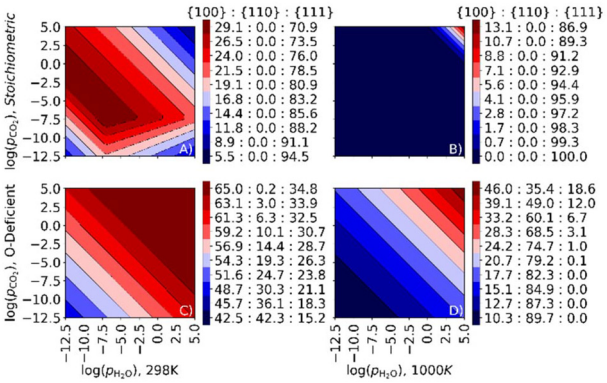

Fig. 10 Ratio between the stoichiometric (A/B) and O-deficient (C/D) {100}, {110} and {111} surfaces as a function of p_{CO_2} and p_{H_2O} for stoichiometric (A/B) and O-deficient (C/D) CeO_2 nanoparticles at fixed temperatures of 298 K (A/C) and 1000 K (B/D).

Relative surface areas in the presence of H_2O

Fig. 9C and D show the predicted area ratios of the {100}, {110} and {111} surface areas as a function of temperature and p_{H_2O} for stoichiometric and O-deficient CeNPs. As for CO_2 adsorption, we predict that {111} surface is dominant, suggesting octahedral particles, with a small proportion of the {100} surface present close to the predicted T_{D,H_2O} for the {111} surface. Unlike with CO_2 adsorption, however, we predict similar behaviour for both the stoichiometric and O-deficient surfaces, with the main difference being the higher T_{D,H_2O} from the latter. As a consequence, the stoichiometric CeNPs are predicted to express bare surfaces above the (relatively low) T_{D,H_2O} for the {111} surface, while the O-deficient CeNPs are predicted to have adsorbed H_2O under a much wider range of conditions.

Ziemba *et al.*[103,104] showed that polycrystalline Au/CeO_2 catalysts with dominant {111} surfaces had higher catalytic activity for the low-temperature water-gas shift reaction than octahedral, cubic and rod-like CeNPs, with the activity falling in the order of octahedral > cubic > rod-like. Since we predict the octahedral CeNPs to be the most stable, we would not expect a catalyst to lose performance over time due to surface reconstruction. Symington *et al.* predicted that O-deficient CeNPs should form truncated octahedra at low temperature.[26] Under conditions of T = 300 K and p_{H_2O} = 1 bar, they predicted a 70 : 0 : 30 ratio of the {111}, {110} and {100}, with H_2O adsorbed to all surfaces, whereas we predict 100% {111} with adsorbed H_2O. The difference may be because the 16.7% coverage modelled in the previous study is lower than the 25% in the present study, and the coverage would impact the relative energies of the three surfaces. This indicates that catalyst design should also consider the surface coverage, as this may influence the stability of a particular morphology.

Relative surface areas in the presence of CO_2 and H_2O

To examine the impact of co-adsorption on the surface area ratio, we plot surface phase diagrams as a function of p_{CO_2} and p_{H_2O} at fixed T = 298 and 1000 K (Fig. 10). In this analysis, comparing the temperature to the selective and simultaneous desorption temperatures at a given set of pressures indicates whether the surface is bare or has CO_2, H_2O or both molecules co-adsorbed.

For the stoichiometric surfaces, under most conditions, we predict a truncated octahedral shape at 298 K and an octahedral shape at 1000 K (Fig. 10A/B). At 298 K and $p_{CO_2} = p_{H_2O}$ = 1 bar, we predict that both H_2O and CO_2 are co-adsorbed to the nanoparticle surface, and that CO_2 desorbs from the stoichiometric {110} and {111} surfaces at $p_{CO_2} < 10^{-9}$ and 10^{-4} bar, respectively, while H_2O desorbs from both surfaces at $p_{H_2O} < 10^{-5}$ bar. At 298 K, we predict a higher proportion of the {100} surface than with individual adsorption of CO_2 or H_2O (*cf.* Fig. 9A/C), indicating that the co-adsorption stabilises this surface and hence favours truncated octahedral over octahedral particles. At 1000 K and $p_{CO_2} = p_{H_2O}$ = 1 bar, we predict bare surfaces and a dominant {111} surface under all conditions except for high adsorbate partial pressures, indicating that the co-adsorption has relatively little effect on the surface area ratios at higher temperature.

Surface phase diagrams for the O-deficient surfaces are shown in Fig. 10C/D. At 298 K and $p_{CO_2} = p_{H_2O}$ = 1 bar, the area ratio of the {100}, {110} and {111} surfaces is 65 : 0.2 : 34.8, which corresponds to a truncated octahedron (Fig. 10C). Under these conditions, CO_2 and H_2O are predicted to be co-adsorbed to all surfaces. At a lower partial pressure of 10^{-10} bar of both adsorbates, the surface area ratio is 51.6 : 24.7 : 23.8, *i.e.,* including a higher proportion of the {110} surface, which implies a complex NP shape with significant proportions of all three surfaces exposed. We predict that both H_2O and CO_2 are adsorbed at the {100} surface, with H_2O but not CO_2 adsorbed at the {110} and {111} surfaces.

At a higher temperature of 1000 K (Fig. 10D) the calculations predict a lower proportion of the {111} surface, and at $p_{CO_2} = p_{H_2O}$ = 1 bar the surface area ratio is 24.2 : 74.8 : 1.0 for the {100} : {110} : {111} surfaces, indicating a rod-like morphology. Under these conditions H_2O remains adsorbed to the

{100} surface but the other two surfaces are bare. The adsorption of H_2O may therefore stabilise the {100} surface.

Predicted particle morphologies

The surface area ratios from the surface phase diagrams provides an indication of the nanoparticle morphologies, but more accurate shapes can be predicted using the Wulff construction.[105] To aid the reader in conceptualising these, Fig. 11A shows an idealised three-component phase diagram of the particle shapes obtained for different relative areas of the {100}, {110} and {111} surfaces, under the assumption that it is possible to obtain all ratios. However, in reality, it is likely that certain area ratios are not thermodynamically stable and would either be difficult to access synthetically and/or unstable to ageing,[25,26,106] resulting in so-called "morphology gaps" analogous to the "solubility gaps" in phase diagrams of three-component alloys.

Based on our calculations, we predict the range of shapes accessible to stoichiometric and O-deficient CeNPs at 298 and 1000 K (Fig. 11B/C and D/E). As for the analysis in Fig. 10, the surface speciation can also be inferred from the calculated desorption temperatures. To aid discussion, we also list in Table 5, which CeNP shapes are predicted to be thermodynamically accessible at both 298 and 1000 K and p_{CO_2}/p_{H_2O} corresponding to low, high and intermediate adsorbate pressures.

Table 5 CeNP shapes predicted to be accessible at T = both 298 K and 1000 K and with three different adsorbate partial pressures p_{CO_2} and p_{H_2O}. ✓ denotes accessible shapes, and X denotes inaccessible shapes.

$\log_{10}(p_{CO_2})$	−12	0	5
$\log_{10}(p_{H_2O})$	−12	0	5
CeNP shape			
	X	X	X
	✓	✓	X
	X	X	X
	X	X	X
	✓	✓	X
	✓	✓	✓
	✓	X	✓
	X	X	X
	X	X	X

At both 298 and 1000 K, we predict that stoichiometric CeNPs will adopt shapes based around truncated octahedra. At 1000 K and $p_{CO_2} = p_{H_2O} = 1$ bar, the {100} surface is bare and therefore destabilised, resulting in a more octahedral shape, whereas at 298 K the adsorption of both molecules and consequent stabilisation results in stronger expression of this

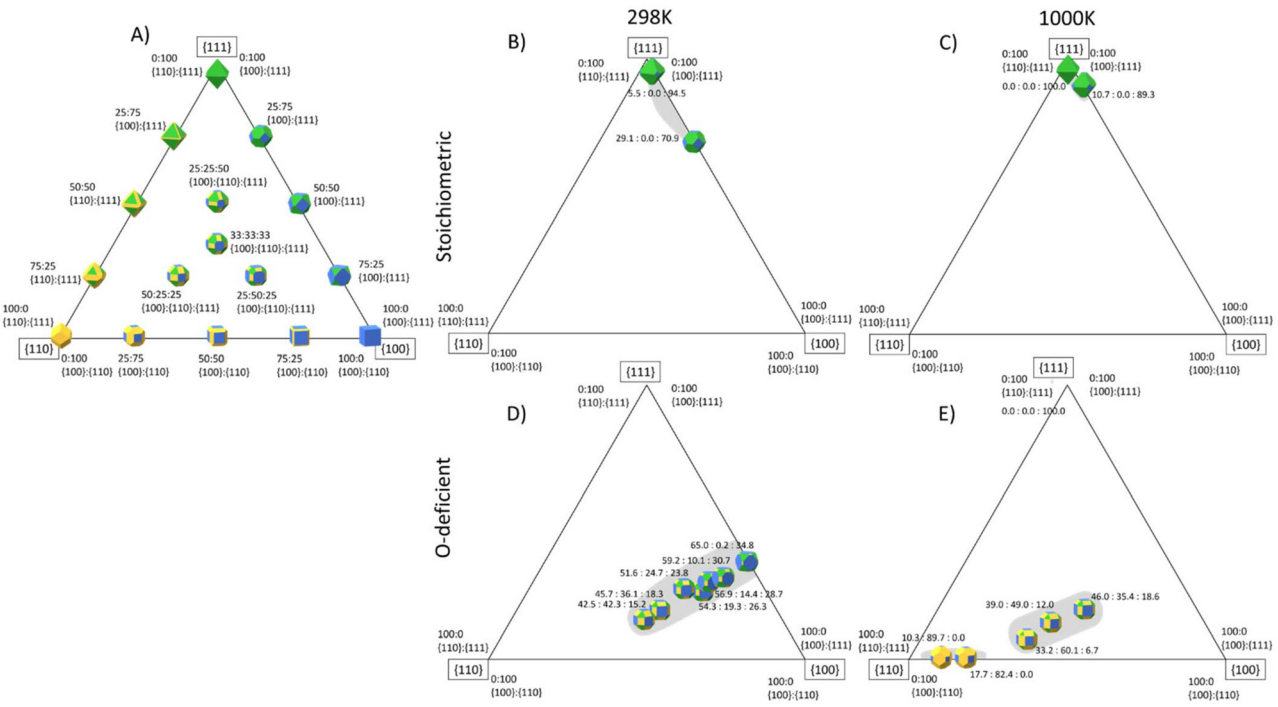

Fig. 11 Predicted particle morphology of ceria nanoparticles (CeNPs) as a function of the relative areas of the {111} (green), {110} (yellow) and {100} surfaces (blue) surfaces. The three corners of the triangle show the shapes of particles formed from single surfaces, the three sides show the shapes obtained with different ratios of two surfaces areas, and points within the triangle show the shapes obtained with different proportions of all three surfaces. (A) Particle morphologies assuming all surface area ratios are accessible. (B)/(C) Stoichiometric CeNP shapes based on the area ratios predicted to be accessible at 298 K (B) and 1000 K (C). (D)/(E) O-deficient CeNP shapes based on the area ratios predicted to be accessible at 298 K (D) and 1000 K (E). In (B)–(E) the grey areas show regions of accessible surface area ratios where the corresponding CeNP shapes are thermodynamically stable. The Wulff constructions were generated using the WulffPack Python package.[110]

surface. On the other hand, for both high $p_{CO_2} = p_{H_2O} = 10^5$ bar and low $p_{CO_2} = p_{H_2O} = 10^{-12}$ bar, we predict a more octahedral morphology with dominant {111} facets.

O-deficient CeNPs are predicted to form truncated octahedra at 298 K and $p_{CO_2} = p_{H_2O} = 1$ bar. Under these conditions, CO_2 and H_2O are adsorbed to all three surfaces. Low adsorbate pressures increase the areas of {110} and {100} surfaces and result in a rhombicuboctahedral shape expressing all three surfaces but with a smaller proportion of the {111} surface. Under these conditions, we predict that H_2O is adsorbed to all three surfaces while CO_2 selectively desorbs from the {110} and {111} surfaces. At 1000 K and $p_{CO_2} = p_{H_2}O = 1$ bar, we predict bare octahedra, whereas at high adsorbate pressures both CO_2 and H_2O are present on the {100} surface, resulting in a larger expression of the {111} and {100} surfaces and a cuboidal-like morphology. This is due to the adsorbates stabilising the {100} surface and is consistent with literature studies showing that the presence of H_2O and CO_2 can stabilise the {100} surface at the expense of the {111} surface.[25,26,35]

Previous work by Aneggi *et al.*[27] predicted a significant effect of temperature on the shapes of CeNPs, and at temperatures above 773 K they predicted similar shapes to those our calculations identify as accessible in Fig. 11B and E.

Predicting particle morphologies is a powerful technique for linking the atomistic surface calculations to experiments. Morphological control is also key to exploiting facet-dependant properties, and studies have shown that the morphology is strongly linked to the catalytic activity.[14,16,17,19,21,27,107]

It has been shown that the particle shape can be controlled through the synthesis, and that it is possible to access shapes that may not be the most thermodynamically preferred.[9–11,14–22] However, over time and under catalytic cycling the nanoparticles will experience a thermodynamic driving force to reconstruct to the most stable structures under their operating conditions. Our predicted morphologies can therefore be used to aid in the design of catalysts and to provide an indication of how ageing might affect long-term performance. For example, Caddeo *et al.*[18] found that nanocubes show the highest redox catalytic ability, due to the greatest expression of reactive {100} surfaces,[108] and our study predicts that such shapes should be accessible under controlled conditions.

Discussion

Finally, we combine our predictions with experimental evidence for which particle shapes/surfaces are best for certain applications to develop some more general guidelines for the design and optimisation of ceria-based catalysts.

The water-gas shift reaction, which converts CO and H_2O to CO_2 and H_2, depends on the presence of surface-bound H_2O but can be deactivated or "poisoned" by the presence of CO_2.[44,48] Nanocubes are expected to promote this reaction as the {100} surface has a higher affinity for H_2O.[49] It has also been demonstrated that CO_2 and H_2O can stabilise {100} over {111} facets and therefore inhibit the formation of more stable octahedral nanoparticles with reduced expression of the desired {100} surface.[26,35] We predict that the proportion of the {100} surface could be enhanced and/or maintained on ageing under O-deficient conditions, suggesting that a reducing environment may be optimal. The selective stabilisation of the {100} surface can be related to the ease with which water can dissociate on this surface, evident from the much lower energy for dissociative compared to molecular adsorption (−2.75 *vs.* −0.7 eV; this energy difference is largest for the {100} surface).

It is also well known that the {100} surface can be "capped" by capping agents that can influence the resulting morphology,[109] and it has been suggested that H_2O could act as such a species. In this scenario, adsorption of H_2O would block mass transport to the {100} surface and preserve the desired cuboidal morphology.[26]

Our calculations support this by showing that H_2O binds strongly to, and therefore difficult to remove from, the {100} surface, and that it can stabilise the {100} surface over the {111} facet. Our calculations further highlight the impact of temperature and adsorbate partial pressure in maintaining this desirable particle morphology. At room temperature and pressure, H_2O is adsorbed to the {100} surface, but under typical high-temperature operation, and assuming some degree of O-deficiency in the surfaces, the operating temperature would need to be kept below 1117 K to maintain the blocking effect. If higher operating temperatures were required, then the partial pressure of H_2O could be increased to compensate.

A second example of where our work may have implications in catalyst design is when using supercritical fluids (SCFs) during synthesis.[111,112] Symington *et al.*[25] predicted that that CeNPs treated in supercritical CO_2 will become nanocubes but did not consider the presence of H_2O. It has been shown that in the presence of supercritical H_2O ceria forms nanocubes. This morphology is desirable because nanocubes have been shown to exhibit high catalytic activity toward the deNOx reaction.[111,113] However, our results suggest that under supercritical H_2O (646 K and $p_{H_2O} = 221$ bar) an octahedral morphology is preferred. This in turn implies that the formation of nanocubes in the experimental studies with supercritical H_2O may be a kinetic effect and that the catalysts may experience a thermodynamic driving force for transformation to an octahedral morphology over time.

Conclusions

In summary, we have outlined a comprehensive theoretical framework for analysing surface speciation and predicting the thermodynamically stable particle morphologies accessible under a given set of environmental conditions. Advances in the synthesis of nanoparticles allow specific morphologies to be targeted, and our methodology complements these efforts by providing a means to determine whether a target shape is thermodynamically stable under the environmental conditions of a given target application. This is critical for catalysis, particularly in higher-temperature processes, where it is essential that the catalysts can undergo multiple catalytic cycles without loss of activity, and, since activity is generally morphology

dependent, nanoparticulate catalysts must maintain their shapes over their lifetime.

In this work we have investigated CeO_2 as an industrially important catalyst. Our methodology allows us to map the thermodynamically stable shapes of CeO_2 nanoparticles as a function of temperature, CO_2 and H_2O adsorbate pressure, and surface composition, which in turn enables thermodynamically-driven evolution to the particle morphology under operating conditions to be anticipated and understood. In particular, we have predicted that co-adsorbed CO_2 and H_2O stabilize the {100} and {110} surfaces, and particularly the O-deficient surfaces, producing cuboidal morphologies. If this morphology is desirable, our modelling therefore suggests conditions to obtain it. Alternatively, our modelling predicts that nanoparticles prepared in other, kinetically trapped morphologies will experience a drive toward reconstruction to this shape during thermal ageing, which could have a detrimental impact on performance if not anticipated.

Finally, we note that the modelling procedure we adopt in this work is general and could be applied to other systems and/or adsorbates, thus providing insight into the nanoparticulate forms of other fluorite materials with similar industrially important applications.

Future studies should focus on increasing the complexity of the DFT calculations by including adsorbates of different nature and their concentration, as well as the complex morphology of nanoparticles surfaces including edges, kinks, and steps. Furthermore, ceria can still maintain its structure and be reduced with very high concentrations of Ce^{3+},[114] and while our protocol will be able to account for all range of oxygen partial pressure, of course this would need to be developed in further research.

Data access statement

Raw data related to this research are available at https://doi.org/10.17632/9hd54s429t

Author contributions

Conceptualization: S. M., S. C. P., M. M.; data curation: S. M., M. M.; formal analysis: S. M., J. S. T., J. M. F., J. M. S., M. M.; funding acquisition: L. J. G., D. J. C., M. M.; investigation: S. M., L. J. G., D. J. C., M. M.; methodology: S. M., J. S. T., A. R. S., J. M. S., M. M.; project administration: M. M.; resources: L. J. G., D. J. C., M. M.; supervision: L. J. G., D. J. C., M. M.; validation: S. M., J. M. S., M. M.; visualization: S. M., J. M. S., L. J. G., D. J. C., S. C. P., M. M.; writing – original draft: S. M., J. M. S., M. M.; writing – review & editing: S. M., A. R. S., J. S. T., J. M. F., J. M. S., L. J. G., D. J. C., S. C. P., M. M.

Conflicts of interest

There are no conflicts to declare.

Acknowledgements

We acknowledge the University of Huddersfield (UoH) EPSRC-DTP competition 2018–19 (EP/R513234/1) for funding SM. JMS is grateful to UK Research and Innovation (UKRI) for the award of a Future Leaders Fellowship (MR/T043121/1), and to the University of Manchester (UoM) for the previous support of a UoM Presidential Fellowship. Calculations were run on the ARCHER and ARCHER2 UK National Supercomputing Services *via* our membership of the UK HEC Materials Chemistry Consortium (MCC; EPSRC EP/L000202/1, EP/R029431/1, EP/X035859/1). Analysis was performed on the Orion and Violeta computing facilities at UoH.

References

1 J. J. Delgado, E. del Río, X. Chen, G. Blanco, J. M. Pintado, S. Bernal and J. J. Calvino, *Catalysis by Ceria and Related Materials*, 2013, 47–138.
2 D. R. Mullins, *Surf. Sci. Rep.*, 2015, **70**, 42–85.
3 L. Vivier and D. Duprez, *ChemSusChem*, 2010, **3**, 654–678.
4 A. S. Karakoti, N. A. Monteiro-Riviere, R. Aggarwal, J. P. Davis, R. J. Narayan, W. T. Seif, J. McGinnis and S. Seal, *JOM*, 2008, **60**, 33–37.
5 T. Montini, M. Melchionna, M. Monai and P. Fornasiero, *Chem. Rev.*, 2016, **116**, 5987–6041.
6 J. Wu, X. Wang, Q. Wang, Z. Lou, S. Li, Y. Zhu, L. Qin and H. Wei, *Chem. Soc. Rev.*, 2019, **48**, 1004–1076.
7 Y. Huang, J. Ren and X. Qu, *Chem. Rev.*, 2019, **119**, 4357–4412.
8 F. Wei, C. J. Neal, T. S. Sakthivel, Y. Fu, M. Omer, A. Adhikary, S. Ward, K. M. Ta, S. Moxon, M. Molinari, J. Asiatico, M. Kinzel, S. N. Yarmolenko, V. San Cheong, N. Orlovskaya, R. Ghosh, S. Seal and M. Coathup, *Bioact. Mater.*, 2023, **21**, 547–565.
9 Z. Tan, G. Li, H. L. Chou, Y. Li, X. Yi, A. H. Mahadi, A. Zheng, S. C. Edman Tsang and Y. K. Peng, *ACS Catal.*, 2020, **10**, 4003–4011.
10 T. Sakthivel, S. Das, A. Kumar, D. L. Reid, A. Gupta, D. C. Sayle and S. Seal, *ChemPlusChem*, 2013, **78**, 1446–1455.
11 M. J. Manto, P. Xie and C. Wang, *ACS Catal.*, 2017, **7**, 1931–1938.
12 C. Yang, X. Yu, S. Heißler, A. Nefedov, S. Colussi, J. Llorca, A. Trovarelli, Y. Wang and C. Wöll, *Angew. Chem., Int. Ed.*, 2017, **56**, 375–379.
13 C. Yang, M. Capdevila-Cortada, C. Dong, Y. Zhou, J. Wang, X. Yu, A. Nefedov, S. Heißler, N. López, W. Shen, C. Wöll and Y. Wang, *J. Phys. Chem. Lett.*, 2020, **11**, 7925–7931.
14 T. X. T. Sayle, M. Molinari, S. Das, U. M. Bhatta, G. Möbus, S. C. Parker, S. Seal and D. C. Sayle, *Nanoscale*, 2013, **5**, 6063–6073.
15 L. M. Morgan, M. Molinari, A. Corrias and D. C. Sayle, *ACS Appl. Mater. Interfaces*, 2018, **10**, 32510–32515.

16 T. X. T. Sayle, M. Cantoni, U. M. Bhatta, S. C. Parker, S. R. Hall, G. Möbus, M. Molinari, D. Reid, S. Seal and D. C. Sayle, *Chem. Mater.*, 2012, **24**, 1811–1821.
17 U. Castanet, C. Feral-Martin, A. Demourgues, R. L. Neale, D. C. Sayle, F. Caddeo, J. M. Flitcroft, R. Caygill, B. J. Pointon, M. Molinari and J. Majimel, *ACS Appl. Mater. Interfaces*, 2019, **11**, 11384–11390.
18 F. Caddeo, A. Casu, D. Loche, L. M. Morgan, G. Mountjoy, C. O'Regan, M. F. Casula, S. Hayama, A. Corrias and A. Falqui, *J. Colloid Interface Sci.*, 2021, **583**, 376–384.
19 F. Polo-Garzon, Z. Bao, X. Zhang, W. Huang and Z. Wu, *ACS Catal.*, 2019, **9**, 5692–5707.
20 Z. L. Wang and X. Feng, *J. Phys. Chem. B*, 2003, **107**, 13563–13566.
21 A. Trovarelli and J. Llorca, *ACS Catal.*, 2017, **7**, 4716–4735.
22 Y. Lin, Z. Wu, J. Wen, K. R. Poeppelmeier and L. D. Marks, *Nano Lett.*, 2014, **14**, 191–196.
23 G. Möbus, Z. Saghi, D. C. Sayle, U. M. Bhatta, A. Stringfellow and T. X. T. Sayle, *Adv. Funct. Mater.*, 2011, **21**, 1971–1976.
24 J. V. Kildgaard, H. A. Hansen and T. Vegge, *Mater. Today Adv.*, 2020, **8**, 100111.
25 A. R. Symington, R. M. Harker, M. T. Storr, M. Molinari and S. C. Parker, *J. Phys. Chem. C*, 2020, **124**, 23210–23220.
26 A. R. Symington, M. Molinari, S. Moxon, J. M. Flitcroft, D. C. Sayle and S. C. Parker, *J. Phys. Chem. C*, 2020, **124**, 3577–3588.
27 E. Aneggi, D. Wiater, C. De Leitenburg, J. Llorca and A. Trovarelli, *ACS Catal.*, 2014, **4**, 172–181.
28 S. Chen, T. Cao, Y. Gao, D. Li, F. Xiong and W. Huang, *J. Phys. Chem. C*, 2016, **120**, 21472–21485.
29 N. Ta, J. Liu, S. Chenna, P. A. Crozier, Y. Li, A. Chen and W. Shen, *J. Am. Chem. Soc.*, 2012, **134**, 20585–20588.
30 K. Zhou and Y. Li, *Angew. Chem., Int. Ed.*, 2012, **51**, 602–613.
31 L. Litti, J. Reguera, F. J. Garciá De Abajo, M. Meneghetti and L. M. Liz-Marzán, *Nanoscale Horiz.*, 2020, **5**, 102–108.
32 P. Zhao, Z. Cao, X. Liu, P. Ren, D. B. Cao, H. Xiang, H. Jiao, Y. Yang, Y. W. Li and X. D. Wen, *ACS Catal.*, 2019, **9**, 2768–2776.
33 P. Stelmachowski, K. Ciura and G. Grzybek, *Catal. Sci. Technol.*, 2016, **6**, 5554–5560.
34 Y. Fu, C. J. Neal, E. Kolanthai, S. Munir, K. M. Ta, M. Molinari and S. Seal, *Colloids Surf., A*, 2023, **679**, 132616.
35 T. Wu, N. López, T. Vegge and H. A. Hansen, *J. Catal.*, 2020, **388**, 1–10.
36 M. Molinari, S. C. Parker, D. C. Sayle and M. S. Islam, *J. Phys. Chem. C*, 2012, **116**, 7073–7082.
37 S. Kumar and P. K. Schelling, *J. Chem. Phys.*, 2006, **125**, 204704.
38 M. Fronzi, S. Piccinin, B. Delley, E. Traversa and C. Stampfl, *Phys. Chem. Chem. Phys.*, 2009, **11**, 9188–9199.
39 A. Röckert, J. Kullgren and K. Hermansson, *J. Chem. Theory Comput.*, 2022, **18**, 7683–7694.
40 X. Sun, E. Vøllestad, P. M. Rørvik, S. Prodinger, G. N. Kalantzopoulos, A. Chatzitakis and T. Norby, *Appl. Surf. Sci.*, 2023, **611**, 155590.
41 K. R. Hahn, M. Iannuzzi, A. P. Seitsonen and J. Hutter, *J. Phys. Chem. C*, 2013, **117**, 1701–1711.
42 Z. Cheng, B. J. Sherman and C. S. Lo, *J. Chem. Phys.*, 2013, **138**, 014702.
43 P. M. Albrecht, D. E. Jiang and D. R. Mullins, *J. Phys. Chem. C*, 2014, **118**, 9042–9050.
44 X. Liu, W. Ruettinger, X. Xu and R. Farrauto, *Appl. Catal., B*, 2005, **56**, 69–75.
45 Z. Wu, M. Li and S. H. Overbury, *J. Catal.*, 2012, **285**, 61–73.
46 M. Nolan and G. W. Watson, *J. Phys. Chem. B*, 2006, **110**, 16600–16606.
47 A. Kumar, S. Das, P. Munusamy, W. Self, D. R. Baer, D. C. Sayle and S. Seal, *Environ. Sci. Nano*, 2014, **1**, 516–532.
48 C. H. Kim and L. T. Thompson, *J. Catal.*, 2005, **230**, 66–74.
49 Z. Tan, Y. Chen, J. Zhang, J. Chou, A. Hu and Y. Peng, *Chem. – Eur. J.*, 2020, **26**, 10598–10606.
50 T. Montini, M. Melchionna, M. Monai and P. Fornasiero, *Chem. Rev.*, 2016, **116**, 5987–6041.
51 J. R. Scheffe, M. Welte and A. Steinfeld, *Ind. Eng. Chem. Res.*, 2014, **53**, 2175–2182.
52 P. Furler, J. R. Scheffe and A. Steinfeld, *Energy Environ. Sci.*, 2012, **5**, 6098–6103.
53 M. Tou, J. Jin, Y. Hao, A. Steinfeld and R. Michalsky, *React. Chem. Eng.*, 2019, **4**, 1431–1438.
54 A. Haeussler, S. Abanades, J. Jouannaux, M. Drobek, A. Ayral and A. Julbe, *AIMS Mater. Sci.*, 2019, **6**, 657–684.
55 G. Kresse and J. Furthmüller, *Phys. Rev. B: Condens. Matter Mater. Phys.*, 1996, **54**, 11169–11186.
56 J. Heyd, G. E. Scuseria and M. Ernzerhof, *J. Chem. Phys.*, 2003, **118**, 8207–8215.
57 J. Heyd, G. E. Scuseria and M. Ernzerhof, *J. Chem. Phys.*, 2006, **124**, 219906.
58 J. P. Perdew, K. Burke and M. Ernzerhof, *Phys. Rev. Lett.*, 1996, **77**, 3865–3868.
59 A. I. Liechtenstein, V. I. Anisimov and J. Zaanen, *Phys. Rev. B: Condens. Matter Mater. Phys.*, 1995, **52**, R5467–R5470.
60 S. L. Dudarev, G. A. Botton, S. Y. Savrasov, C. J. Humphreys and A. P. Sutton, *Phys. Rev. B: Condens. Matter Mater. Phys.*, 1998, **57**, 1505–1509.
61 M. Nolan, S. Grigoleit, D. C. Sayle, S. C. Parker and G. W. Watson, *Surf. Sci.*, 2005, **576**, 217–229.
62 M. Nolan, S. C. Parker and G. W. Watson, *Surf. Sci.*, 2005, **595**, 223–232.
63 D. O. Scanlon, N. M. Galea, B. J. Morgan and G. W. Watson, *J. Phys. Chem. C*, 2009, **113**, 11095–11103.
64 J. Paier, C. Penschke and J. Sauer, *Chem. Rev.*, 2013, **113**, 3949–3985.
65 X. Zhang, L. Zhu, Q. Hou, J. Guan, Y. Lu, T. W. Keal, J. Buckeridge, C. R. A. Catlow and A. A. Sokol, *Chem. Mater.*, 2023, **35**, 207–227.

66 X. Zhang, T. Liu, L. Zhu, J. Guan, Y. Lu, T. W. Keal, J. Buckeridge, C. R. A. Catlow and A. A. Sokol, *Angew. Chem., Int. Ed.*, 2023, **62**, e202308411.
67 D. Fernández-Torre, K. Kośmider, J. Carrasco, M. V. Ganduglia-Pirovano and R. Pérez, *J. Phys. Chem. C*, 2012, **116**, 13584–13593.
68 C. Artini, M. Pani, M. M. Carnasciali, J. R. Plaisier and G. A. Costa, *Inorg. Chem.*, 2016, **55**, 10567–10579.
69 Y. Ma, Y. Ma, G. Giuli, H. Euchner, A. Groß, G. O. Lepore, F. d'Acapito, D. Geiger, J. Biskupek, U. Kaiser, H. M. Schütz, A. Carlsson, T. Diemant, R. J. Behm, M. Kuenzel, S. Passerini and D. Bresser, *Adv. Energy Mater.*, 2020, **10**, 2000783.
70 D. J. M. Bevan, *J. Inorg. Nucl. Chem.*, 1955, **1**, 49–59.
71 J. L. F. Da Silva, *Phys. Rev. B: Condens. Matter Mater. Phys.*, 2007, **76**, 193108.
72 P. M. Oliver, S. C. Parker and W. C. Mackrodt, *Modell. Simul. Mater. Sci. Eng.*, 1993, **1**, 755.
73 G. W. Watson, E. T. Kelsey, N. H. de Leeuw, D. J. Harris and S. C. Parker, *J. Chem. Soc., Faraday Trans.*, 1996, **92**, 433–438.
74 A. Symington, J. Tse, M. Molinari, A. Marmier and S. Parker, *J. Open Source Softw.*, 2019, **4**, 1210–1211.
75 K. Momma and F. Izumi, *J. Appl. Crystallogr.*, 2011, **44**, 1272–1276.
76 J. S. Tse, M. Molinari, S. C. Parker and A. R. Symington, *J. Open Source Softw.*, 2022, **7**, 4014.
77 J. S. Tse, J. Grant, J. M. Skelton, L. J. Gillie, R. Zhu, G. L. Pesce, R. J. Ball, S. C. Parker and M. Molinari, *Phys. Chem. Chem. Phys.*, 2023, **25**, 18011–18022.
78 R. Tran, Z. Xu, B. Radhakrishnan, D. Winston, W. Sun, K. A. Persson and S. P. Ong, *Sci. Data*, 2016, **3**, 160080.
79 C.-Y. Zhou, D. Wang and X.-Q. Gong, *Phys. Chem. Chem. Phys.*, 2019, **21**, 19987–19994.
80 K. M. Ta, D. J. Cooke, L. J. Gillie, S. C. Parker, S. Seal, P. B. Wilson, R. M. Phillips, J. M. Skelton and M. Molinari, *J. Phys. Chem. C*, 2023, **127**, 20183–20193.
81 M. Molinari, A. R. Symington, D. C. Sayle, T. S. Sakthivel, S. Seal and S. C. Parker, *ACS Appl. Bio Mater.*, 2019, **2**, 1098–1106.
82 C. Yang, F. Bebensee, J. Chen, X. Yu, A. Nefedov and C. Wöll, *ChemPhysChem*, 2017, **18**, 1874–1880.
83 J. Zhang, X.-Q. Gong and G. Lu, *Surf. Sci.*, 2015, **632**, 164–173.
84 T. X. T. Sayle, S. C. Parker and C. R. A. Catlow, *Surf. Sci.*, 1994, **316**, 329–336.
85 R. Farra, S. Wrabetz, M. E. Schuster, E. Stotz, N. G. Hamilton, A. P. Amrute, J. Pérez-Ramírez, N. López and D. Teschner, *Phys. Chem. Chem. Phys.*, 2013, **15**, 3454–3465.
86 D. R. Mullins, P. M. Albrecht, T.-L. Chen, F. C. Calaza, M. D. Biegalski, H. M. Christen and S. H. Overbury, *J. Phys. Chem. C*, 2012, **116**, 19419–19428.
87 B. Chen, Y. Ma, L. Ding, L. Xu, Z. Wu, Q. Yuan and W. Huang, *J. Phys. Chem. C*, 2013, **117**, 5800–5810.
88 M. B. Watkins, A. S. Foster and A. L. Shluger, *J. Phys. Chem. C*, 2007, **111**, 15337–15341.
89 S. Gritschneder and M. Reichling, *Nanotechnology*, 2007, **18**, 044024.
90 M. A. Henderson, C. L. Perkins, M. H. Engelhard, S. Thevuthasan and C. H. F. Peden, *Surf. Sci.*, 2003, **526**, 1–18.
91 V. Matolín, I. Matolínová, F. Dvořák, V. Johánek, J. Mysliveček, K. C. Prince, T. Skála, O. Stetsovych, N. Tsud, M. Václavů and B. Šmíd, *Catal. Today*, 2012, **181**, 124–132.
92 M. W. Chase, *NIST-JANAF Thermochemical Tables*, NIST, American Institute of Physics, 4th edn, 1998.
93 S. Moxon, A. R. Symington, J. S. Tse, J. Dawson, J. M. Flitcroft, S. C. Parker, D. J. Cooke, R. M. Harker and M. Molinari, *Phys. Chem. Chem. Phys.*, 2020, **22**, 7728–7737.
94 S. D. Senanayake and D. R. Mullins, *J. Phys. Chem. C*, 2008, **112**, 9744–9752.
95 S. D. Senanayake, D. Stacchiola, J. Evans, M. Estrella, L. Barrio, M. Pérez, J. Hrbek and J. A. Rodriguez, *J. Catal.*, 2010, **271**, 392–400.
96 L. Kundakovic, D. R. Mullins and S. H. Overbury, *Surf. Sci.*, 2000, **457**, 51–62.
97 T. Staudt, Y. Lykhach, N. Tsud, T. Skála, K. C. Prince, V. Matolín and J. Libuda, *J. Catal.*, 2010, **275**, 181–185.
98 G. S. Herman, Y. J. Kim, S. A. Chambers and C. H. F. Peden, *Langmuir*, 1999, **15**, 3993–3997.
99 A. Barroso Bogeat, G. Blanco, J. M. Pintado, D. Goma and J. J. Calvino Gámez, *Surf. Interfaces*, 2021, **26**, 101353.
100 N. Hashimoto, K. Mori, K. Asahara, S. Shibata, H. Jida, Y. Kuwahara and H. Yamashita, *Langmuir*, 2021, **37**, 5376–5384.
101 M. Nolan, S. C. Parker and G. W. Watson, *J. Phys. Chem. B*, 2006, **110**, 2256–2262.
102 P. R. L. Keating, D. O. Scanlon and G. W. Watson, *J. Phys.: Condens. Matter*, 2009, **21**, 405502.
103 M. Ziemba, M. V. Ganduglia-Pirovano and C. Hess, *Faraday Discuss.*, 2021, **229**, 232–250.
104 M. Ziemba, C. Schilling, M. V. Ganduglia-Pirovano and C. Hess, *Acc. Chem. Res.*, 2021, **54**, 2884–2893.
105 G. Wulff, *Z. Kristallogr. – Cryst. Mater.*, 1901, **34**, 449–530.
106 D. C. Sayle, F. Caddeo, L. M. Morgan, R. L. Neale, T. X. T. Sayle, C. Brambila, J. Nutter, U. Bhatta, K. M. Ta, J. M. Flitcroft, T. S. Sakthivel, S. Seal, G. Möbus and M. Molinari, *Nano Today*, 2023, **51**, 101916.
107 K. Zhou, X. Wang, X. Sun, Q. Peng and Y. Li, *J. Catal.*, 2005, **229**, 206–212.
108 H. X. Mai, L. D. Sun, Y. W. Zhang, R. Si, W. Feng, H. P. Zhang, H. C. Liu and C. H. Yan, *J. Phys. Chem. B*, 2005, **109**, 24380–24385.
109 M. J. Davies, P. R. Kenway, P. J. Lawrence, S. C. Parker, W. C. Mackrodt and P. W. Tasker, *J. Chem. Soc., Faraday Trans. 2*, 1989, **85**, 555–563.

110 M. J. Rahm and P. Erhart, *J. Open Source Softw.*, 2020, **5**, 1944.
111 T. Adschiri, Y.-W. Lee, M. Goto and S. Takami, *Green Chem.*, 2011, **13**, 1380–1390.
112 M. K. M. Lane and J. B. Zimmerman, *Green Chem.*, 2019, **21**, 3769–3781.
113 J. Zhang, H. Kumagai, K. Yamamura, S. Ohara, S. Takami, A. Morikawa, H. Shinjoh, K. Kaneko, T. Adschiri and A. Suda, *Nano Lett.*, 2011, **11**, 361–364.
114 X. Hao, A. Yoko, C. Chen, K. Inoue, M. Saito, G. Seong, S. Takami, T. Adschiri and Y. Ikuhara, *Small*, 2018, **14**, 1802915.
115 A. S. Pugazhendhi, C. J. Neal, K. M. Ta, M. Molinari, U. Kumar, F. Wei, E. Kolanthai, A. Ady, C. Drake, M. Hughes, S. Yooseph, S. Seal and M. J. Coathup, *Biomater.*, 2024, **307**, 122527.
116 N. Anwar, R. M. Harker, M. T. Storr, M. Molinari and C. K. Skylaris, *Comput. Mater. Sci.*, 2023, **229**, 112396.